Engineering xxx (xxxx) xxx

Contents lists available at ScienceDirect

Engineering

journal homepage: www.elsevier.com/locate/eng

Research
Energy Batteries—Review

Current Applications and Development Status of Anode Materials with 3D Nanostructures for Sodium-Ion Batteries

Honglin Ren, Zihan Zhou, Feng Wu, Siyuan Liu, Guoqiang Tan *, Xinyi Tan *

Beijing Key Laboratory of Environmental Science and Engineering, School of Materials Science and Engineering, Beijing Institute of Technology, Beijing 100081, China

ARTICLE INFO

Article history:
Received 30 December 2024
Revised 7 August 2025
Accepted 20 August 2025
Available online xxxx

Keywords:
Sodium-ion batteries
Anode materials
Microstructure

ABSTRACT

Sodium-ion batteries (SIBs) are considered strong alternatives to lithium-ion batteries (LIBs) because of their low cost and the abundance of sodium resources. However, their commercialization is limited by their low capacity, poor cycling stability, and unfavorable redox potentials. Recent advancements have been made in SIBs anode materials, including alloy-based, carbon-based, and three-dimensional (3D) nanostructured materials. Despite these improvements, SIBs anode materials still suffer from an unstable cycle life and slow kinetics. This review focuses on 3D nanostructured anode materials for SIBs. The advantages of various 3D anode materials and their optimization strategies are summarized. In addition, we discuss the potential of developing high-performance SIB anode materials.

© 2026 THE AUTHORS. Published by Elsevier LTD on behalf of Chinese Academy of Engineering and Higher Education Press Limited Company. This is an open access article under the CC BY-NC-ND license (http://creativecommons.org/licenses/by-nc-nd/4.0/).

1. Introduction

The increasing global energy demand has deepened the dependence on fossil fuels, driving pollution and greenhouse gas emissions. Advancing clean and renewable energy is thus an urgent imperative for combating these environmental challenges [1,2]. Research into lithium-ion batteries (LIBs) began in the early 1980s and led to their commercialization in the 1990s. Owing to their high energy density and long cycle life, LIBs have dominated the portable electronics market and driven advances in mobile communications, computing, electric vehicles, and energy storage systems. Research on sodium-ion batteries (SIBs) emerged at around the same time, exploring them as alternative electrochemical energy storage devices [3,4]. SIBs initially received limited attention because of their lower energy density than LIBs. However, since the 2010s, interest in SIBs has resurged, driven by the scarcity of lithium resources and the resulting economic and geopolitical challenges hindering the sustainable development of LIB technology [5–8].

Both Li and Na are Group I elements and share similar chemical properties, including comparable redox potentials $E_{Na^+/Na} = +2.71$ V (vs standard hydrogen electrode (SHE) and $E_{Li^+/Li} = +3.04$ V vs SHE). Earth's sodium reserves (2.8 wt%) are significantly more abundant than its lithium reserves (0.0017 wt %), highlighting the greater availability of sodium as a resource [9]. The inability of sodium to alloy with aluminum allows SIBs to use aluminum foil as a cost-effective alternative to copper for current collectors [10], reducing material costs from 1.2 to 0.3 USD·m^{-2} [11]. Although current collectors comprise only ~3% of the total battery cost, this substitution contributes meaningfully to the overall savings. Moreover, aluminum improves the chemical stability at 0 V, mitigating the risks of overheating and thermal runaway, which are key to safe transport, thereby enhancing both the economic and commercial viability of SIBs [12].

The operation of SIBs involves the reversible insertion and extraction of Na^+ ions between the cathode and anode, facilitated by their migration through the electrolyte. During charging, Na^+ is extracted from the cathode, moved through the electrolyte, passed through the separator, and intercalated into the anode. During discharging, Na^+ is extracted from the anode and returns to the cathode via the electrolyte and separator, whereas electrons flow through the external circuit to deliver power. This cyclic process enables the charge–discharge functionality of the battery.

Carbon is the most prevalent and commercially viable anode material for LIBs and SIBs. However, the larger ionic radius of Na^+ (1.04 Å) compared to Li^+ (0.76 Å) restricts the applicability of graphite in SIBs due to insufficient interlayer spacing. By contrast, hard carbon in its amorphous form offers a structurally versatile matrix capable of accommodating Na^+ through multiple mechanisms. Its Na^+ storage performance is governed by: ① surface area,

* Corresponding authors.
E-mail addresses: tan123@bit.edu.cn (G. Tan), xinyitan@bit.edu.cn (X. Tan).

https://doi.org/10.1016/j.eng.2025.08.048
2095-8099/© 2026 THE AUTHORS. Published by Elsevier LTD on behalf of Chinese Academy of Engineering and Higher Education Press Limited Company.
This is an open access article under the CC BY-NC-ND license (http://creativecommons.org/licenses/by-nc-nd/4.0/).

Please cite this article as: H. Ren, Z. Zhou, F. Wu et al., Current Applications and Development Status of Anode Materials with 3D Nanostructures for Sodium-Ion Batteries, Engineering, https://doi.org/10.1016/j.eng.2025.08.048

with larger areas enhancing adsorption [13,14]; ② defective sites, including vacancies and heteroatoms, which facilitate ion capture [15]; ③ interlayer insertion, occurring either in a controlled or disordered manner [16], and ④ pore confinement, where Na^+ forms quasi-metallic clusters, with storage capacity closely tied to pore size distribution and total volume [17,18].

Hard carbon, which is constrained by a relatively low theoretical specific capacity, faces challenges in satisfying the growing demand for high-capacity SIBs. To overcome this limitation, alternative sodium storage mechanisms such as alloying and conversion reactions have been explored. These approaches hold significant promise for improving the energy density of SIBs [19,20]. Certain Groups 14 and 15 elements (e.g., Sn, Sb, and P), including metals, metalloids, and non-metals, as well as their compounds (e.g., oxides and sulfides), can undergo alloying or conversion-alloying reactions with sodium, leading to enhanced capacity. Because alloy- and conversion-type anodes generally involve multielectron transfer during reactions with sodium ions, each alloy atom can react with several sodium ions. The general alloying reaction can be represented as $x\mathrm{Na}^+ + x\mathrm{e}^- + \mathrm{M} \leftrightarrow \mathrm{Na}_x\mathrm{M}$, where M represents the alloying element (e.g., Sn, Sb, and P) or the active species derived from their compounds.

In addition, compared to intercalated anode materials, alloy-type anodes react more fully with sodium ions during charge–discharge cycles. This multielectron reaction considerably enhances the theoretical specific capacity of the materials involved. Furthermore, alloy-type materials have a relatively low electrochemical potential when embedded with sodium ions, which facilitates high-capacity discharge at low voltages. This characteristic enables the batteries to effectively utilize the high capacity of the material across the operating voltage range.

Despite the high theoretical capacities of alloy- and conversion-type anodes, their practical use in SIBs faces significant challenges (Table 1) [12,21–30]. A primary obstacle to commercialization is the pronounced capacity decay observed during cycling [31,32]. The key challenge of alloy-based anodes is their substantial volume fluctuations during cycling. Repeated expansion from Na_xM formation during discharging and contraction upon charging induces structural degradation, active material loss, and capacity fading. These stresses lead to cracking, pulverization, and loss of electrical contact, thereby undermining the stability and lifespan. Furthermore, continuous solid electrolyte interface (SEI) formation on fresh surfaces thickens the interface, impeding charge transfer and diminishing the Coulombic efficiency [33–37]. In addition, certain alloy-based anodes, such as those made of P, have poor electrical conductivity, which further limits their specific capacity and performance [3,38–41]. Extensive efforts to enhance alloy-based anodes have focused on nanostructure design and integration with conductive carbon frameworks such as nanofibers and graphene. These strategies collectively boost electron transport, accelerate ion diffusion, and stabilize reaction kinetics, thereby mitigating capacity loss during cycling.

Herein, the research progress on SIBs anode materials with different three-dimensional (3D) microstructures is examined. Unlike most reviews that classify anode materials based on their Na storage mechanisms, this review focuses on the 3D microstructures of the anode materials. The characteristics and preparation methods of anode materials with different structures are summarized, opportunities and challenges associated with each structure are analyzed, and forecasts for the 3D microstructures of future SIBs anode materials are provided.

2. Different microstructures of anode materials

2.1. 3D carbon-host microstructures

The use of 3D carbon-host microstructures as anode materials in SIBs offers several considerable advantages [42]. ① These microstructures create a continuous conductive network that enhances the electrical conductivity of the anodes. This improvement facilitates efficient electron transport during charge–discharge cycles, thereby enhancing the overall battery performance [43,44]. ② 3D carbon hosts offer a flexible matrix that can accommodate the volume changes of alloy-based anodes (e.g., Sn [21] and Sb [23]) in SIBs [45,46]. ③ The high surface area of the 3D carbon architectures improves the interfacial contact between the electrolyte and the active material, thereby enhancing the Na^+ diffusion kinetics and significantly boosting the rate capability of SIBs [46,47]. ④ 3D carbon hosts with diverse morphologies and properties can be designed by adjusting the synthesis parameters. This enables the optimization of anode materials to attain the optimal performance tailored to specific applications [48,49]. Therefore, 3D carbon-host microstructures are widely used in SIBs.

The fabrication methods for the 3D carbon-host microstructures are listed Fig. 1. Template-assisted methods include the use of templates such as metal foams, polymers, or silica, which are subsequently removed to create a 3D porous carbon structure [50–53]. Chemical vapor deposition (CVD) involves growing carbon materials on substrates to form a 3D structure [54,55]. Self-assembly is achieved via the self-assembly properties of carbon precursors such as graphene oxide to form 3D networks [56,57]. Finally, solvothermal methods involve employing solvothermal processes to synthesize carbon materials with an accurately controlled morphology [48,49,53].

2.1.1. Template-assisted methods

The template-assisted method provides significant advantages for the preparation of highly ordered, structurally specific 3D carbon-host materials (Fig. 2(a)). By choosing various template materials and preparation methods, 3D carbon structures with high specific surface areas (SSAs) and tunable pore architectures can be engineered. This method enables the fabrication of carbon materials with ordered structures, making it ideal for preparing porous carbon materials with periodic arrangements. Finally, various types of template materials such as soft, hard, and polymer templates can be selected based on the specific properties required for the final carbon material (Table 2) [50,58–64].

The template-assisted method involves four critical factors. ① Template characteristics, such as pore size and thermal stability, influence the structural integrity and performance of the derived carbon materials and require careful selection. ② Incomplete template removal can degrade the material structure and electro-

Table 1
Alloying mechanisms in SIBs [12].

Alloy system	Fully alloyed phase	Theoretical capacity ($mA{\cdot}h{\cdot}g^{-1}$)	Volume expansion (%)	Average voltage (V vs Na^+/Na)
Sn	$Na_{15}Sn_4$	847	420 [21]	~0.20 [22]
Sb	Na_3Sb	660	390 [23]	~0.60 [24]
Ge	NaGe	567	205 [25]	~0.30 [26]
P	Na_3P	2596	>300 [27]	~0.40 [28]
Bi	Na_3Bi	385	250 [29]	~0.55 [30]

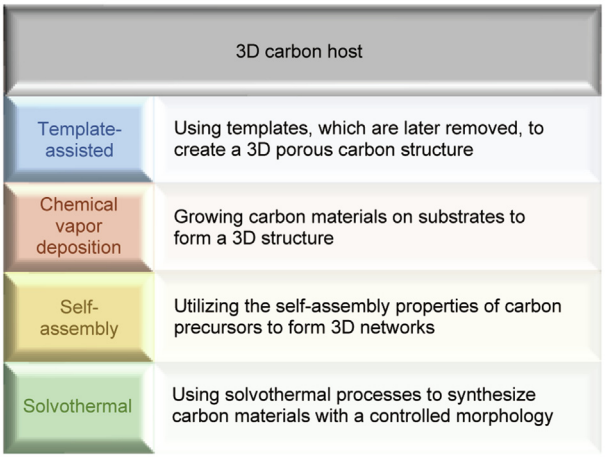


Fig. 1. Fabrication techniques for 3D carbon-host microstructures.

chemical behavior. ③ The choice of the carbon precursor affects the material properties, with the selection tailored for specific applications. ④ The multistage fabrication process, including template synthesis, carbonization, and removal, requires strict control of the parameters at each stage to maintain the material quality.

In addition, for large-scale production, template preparation becomes more costly and complex, which raises the overall production cost. Maintaining template consistency is essential to ensure the stability and reproducibility of the preparation process.

Using a metallic salt as a template provides two-dimensional (2D) confinement that enhances structural integrity and promotes the formation of a porous carbon network, facilitating ion and electron transport while mitigating alloy aggregation and volume change [65–67]. Liang et al. [50] demonstrated that 2D-$MoTe_2$@3D porous carbon networks (3DPCN) (Fig. 2(b)) prepared using NaCl as a template, exhibited an excellent electrochemical performance. Wen et al. [61] employed zinc gluconate as a template to precisely control the microporous structure of hard carbon, thereby enhancing its SSA and pore volume, and improving the performance of SIBs. Gao et al. [62] employed a KCl/K_2SO_4 mixed salt as a template for the preparation of nitrogen/sulfur-doped porous carbon (ECSK-15), augmenting the number of ionic diffusion channels and increasing the ionic exchange rate.

Metal–organic frameworks (MOFs), composed of transition metals and organic ligands, serve as effective organic hard templates in template-assisted methods. Unlike inorganic templates, MOFs retain their ordered pore architecture during pyrolysis [68], allowing precise control over pore size and porosity. Furthermore, heteroatoms from organic ligands are doped into the resulting carbon matrix, and density functional theory (DFT) analysis has confirmed that such doping enhances Na^+ storage, accelerates diffusion, and improves the overall performance. Therefore, the cycling performance of anode materials (e.g. CoP–C@MoS_2/C, as shown in Fig. 2(c)) [58] synthesized using MOFs as templates is exceptional. Lu et al. [63] fabricated $CoTe_2$ nanoparticles within the framework of a graphene aerogel using Co-MOF as a template and adopted an *in situ* growth approach, thereby enhancing ion diffusion and the electrochemical performance. Yu et al. [59] synthesized double-shell and hierarchical N-doped carbon nanocages (DHNCNs) using zeolitic imidazolate framework (ZIF)-8 and dopamine hydrochloride as precursors (Fig. 2(d)). The outer mesoporous and inner microporous layers synergistically enhanced the stability and ion transport, whereas N doping introduced defects and active sites to boost the electrochemical performance.

Soft templates, which are widely used in template-assisted methods, operate at relatively low temperatures and reduce energy consumption, while preserving structural integrity. Their organic nature allows for easy removal with minimal disruption and enables elemental doping, enhancing interfacial interactions, precursor distribution, and nanoscale precision. Zhang et al. [64] used F127, a polyglycol-*block*-propylene glycol copolymer, as a soft template and *N*-allyl thiourea as a precursor for heteroatom doping to synthesize dual-doped N/S porous frameworks (DF-N/S). This approach effectively integrated templating and heteroatom doping strategies, enabling the precise tuning of the structure and composition of the material for enhanced performance. Ou et al. [60] employed polyvinylpyrrolidone (PVP) as a soft template to incorporate Ni_2P with N, P, and S doping (Fig. 2(e)), thereby enhancing

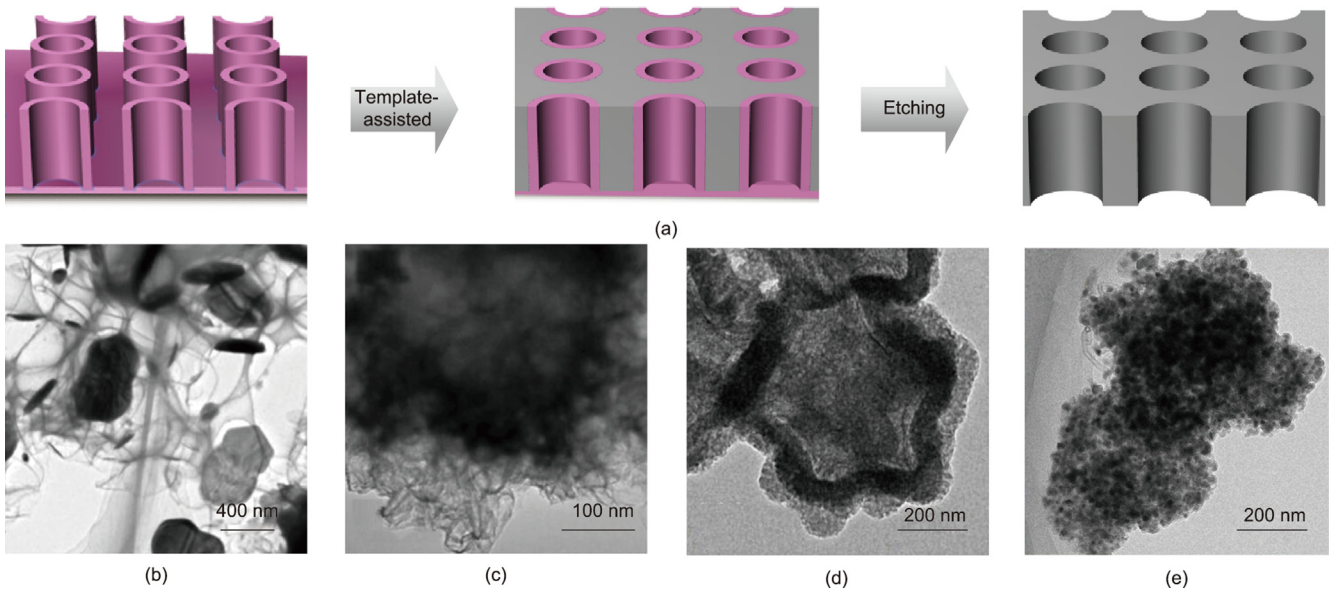


Fig. 2. (a) Schematic of the synthesis process of template assisted. (b–e) Transmission electron microscopy (TEM) images of (b) two-dimensional (2D)-$MoTe_2$@3D porous carbon networks (3DPCN), (c) CoP–C@MoS_2/C, (d) double-shell and hierarchical N-doped carbon nanocages (DHNCNs), and (e) Ni_2P@triple heteroatom (N, P, S)-doped carbon network (NPS). (b) Reproduced from Ref. [50] with permission; (c) reproduced from Ref. [58] with permission; (d) reproduced from Ref. [59] with permission; (e) reproduced from Ref. [60] with permission.

Table 2
Electrochemical performances of 3D carbon-host anode materials for SIBs prepared using template-assisted methods.

Anode	Capacity ($mA{\cdot}h{\cdot}g^{-1}$)	Cycle	Retention	Year	Ref.
2D-$MoTe_2$@3DPCN	412 at 0.1 $A{\cdot}g^{-1}$	100	97.4% at 0.5 $A{\cdot}g^{-1}$	2022	[50]
HC-ZGl + 0.5S	374 at 0.03 $A{\cdot}g^{-1}$	500	90.7% at 0.6 $A{\cdot}g^{-1}$	2024	[61]
ECSK-15	310 at 0.05 $A{\cdot}g^{-1}$	1000	65.24% at 2.0 $A{\cdot}g^{-1}$	2024	[62]
CoP–C@MoS_2/C	414 at 0.1 $A{\cdot}g^{-1}$	1000	90.16% at 1.0 $A{\cdot}g^{-1}$	2023	[58]
NSGA/$CoTe_2$@NPC	697.6 at 0.1 $A{\cdot}g^{-1}$	5000	>99% at 5.0 $A{\cdot}g^{-1}$	2025	[63]
DHNCN	332 at 0.02 $A{\cdot}g^{-1}$	450	887.3% at 0.5 $A{\cdot}g^{-1}$	2024	[59]
DF-N/S-8-2	327 at 0.05 $A{\cdot}g^{-1}$	100	~90% at 0.5 $A{\cdot}g^{-1}$	2024	[64]
Ni_2P@NPS	976.1 at 0.1 $A{\cdot}g^{-1}$	1000	~90% at 6.0 $A{\cdot}g^{-1}$	2025	[60]

HC: hard carbon; ZGl: zinc gluconate; ECSK-15: nitrogen/sulfur-doped porous carbon; NSGA: N- and S-doped graphene aerogel framework; NPC: N-doped porous carbon; DF-N/S: dual-doped N/S porous frameworks.

the electrochemical performance of the material by improving the electron transport and ion storage capabilities.

Overall, template-assisted strategies provide a versatile platform for constructing highly ordered 3D carbon frameworks. By precisely tuning the template properties and fabrication parameters, enhanced Na^+ storage performance can be achieved, offering promising directions for large-scale and high-performance SIBs.

2.1.2. Chemical vapor deposition

CVD has several distinct advantages for synthesizing 3D carbon-host materials (Fig. 3(a)). First, it produces defect-free, uniform, high-purity, and high-quality carbon materials, making it ideal for fabricating advanced carbon nanotubes and graphene. Second, by carefully adjusting parameters such as the reaction gas composition, temperature, and deposition duration, CVD allows precise control of the morphology, dimensions, and porosity of the material. Finally, CVD supports the large-scale production of 3D carbon-host materials in a short timeframe, ensuring exceptional uniformity and making it suitable for industrial applications (Table 3) [54,69–74].

When using CVD to synthesize carbon-host materials, the key factors to consider include ① careful control of reaction gases, flow rates, and concentrations to ensure high-quality deposition; ② precise thermal management to prevent defects from temperature extremes; ③ optimal deposition duration to balance thickness and structural integrity; ④ selecting substrates with suitable thermal and electrical properties for uniform deposition; ⑤ proper substrate cleaning to eliminate impurities; and ⑥ adhering to safety measures to prevent gas leaks and effectively manage byproducts.

Because of the high purity and uniform thickness of the carbon layer produced via CVD, it can be uniformly coated on the surface of materials, thereby enhancing their electrical conductivity, provided that an appropriate substrate material is selected. For example, the 3D metallic phase (1T)-SnS_2/reduced graphene oxide (rGO) composite prepared by Li et al. [72] demonstrated excellent initial specific capacity (768.8 $mA{\cdot}h{\cdot}g^{-1}$) and remarkable reversibility. Chen et al. [69] performed a carbon coating modification on the surface of $Zn_3(PO_4)_2$ (ZPO) through CVD to obtain ZPO@C composites (Fig. 3(b)). The modified composites exhibited outstanding electrochemical performance. Zhou et al. [70] utilized treated pyrolytic carbon black (TCBp) derived from waste tires as a precursor and synthesized TCBp@vertical graphene nanosheet (VGS) composites (Fig. 3(c)) by coating their surface with VGSs via CVD. This approach enhances the value of waste tires, while offering significant economic and environmental advantages. Additionally, CVD offers unique advantages for the fabrication of carbon nanostructures and graphene, providing high-purity, high-quality, and defect-free carbon materials. Tan et al. [54] synthesized Sn_4P_3/-graphene tubes (GT), as shown in Fig. 3(d). These GT consisted of hydrophilic inner and hydrophobic outer graphene layers, which restricted the growth of Sn_4P_3 nanoparticles into the hydrophilic inner tubes during hydrothermal synthesis and prevented growth

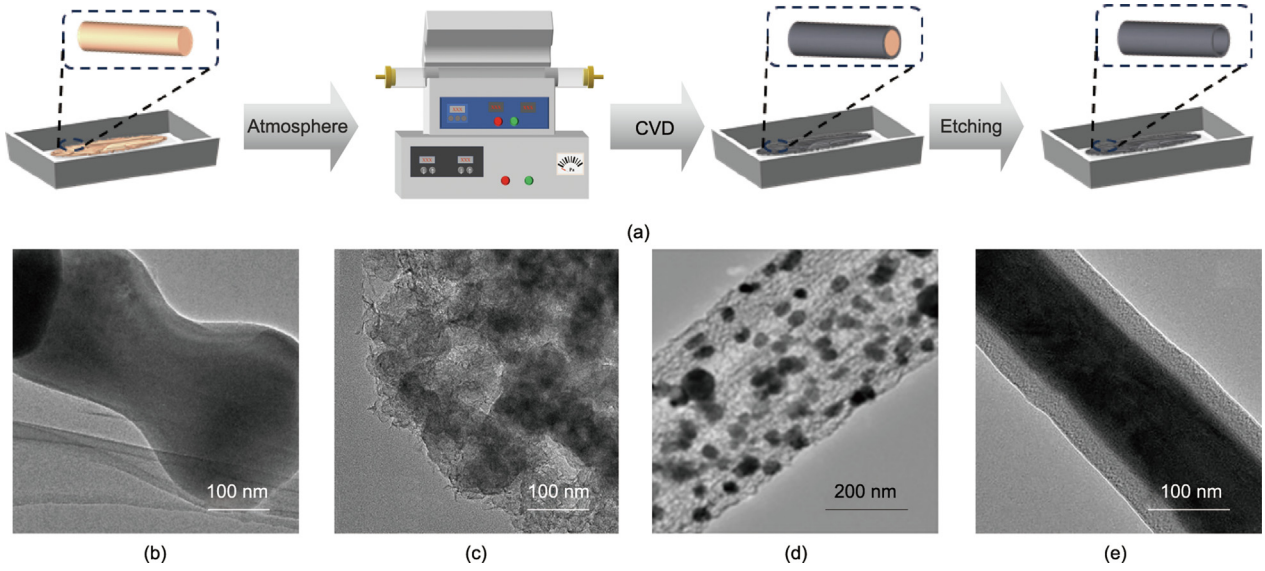


Fig. 3. (a) Schematic of the synthesis process using CVD. (b–e) TEM images of (b) $Zn_3(PO_4)_2$ (ZPO)@C, (c) treated pyrolytic carbon black (TCBp)@vertical graphene nanosheet (VGS), (d) Sn_4P_3/graphene tubes (GT) composite, and (e) Fe_2P@C. (b) Reproduced from Ref. [69] with permission; (c) reproduced from Ref. [70] with permission; (d) reproduced from Ref. [54] with permission; (e) reproduced from Ref. [71] with permission.

Table 3
Electrochemical performances of 3D carbon-host anode materials in SIBs prepared using CVD.

Anode	Capacity ($mA·h·g^{-1}$)	Cycle	Retention	Year	Ref.
3D 1T-SnS_2/rGO	865.6 at 0.1C	100	84.6% at 0.5C	2022	[72]
ZPO@C	315.7 at 0.1C	400	60% at 10C	2025	[69]
TCBp@VGSs	305.9 at 0.1 $A·g^{-1}$	1900	~100% at 1.0 $A·g^{-1}$	2024	[70]
Sn_4P_3/GT	821 at 0.2 $A·g^{-1}$	500	>90% at 0.5 $A·g^{-1}$	2022	[54]
CNF	288.6 at 0.05 $A·g^{-1}$	700	~92% at 0.05 $A·g^{-1}$	2025	[73]
Fe_2P@C	~440 at 0.05 $A·g^{-1}$	1400	80.25% at 1.5 $A·g^{-1}$	2023	[71]
Fe–Fe_3C@GC	430.1 at 0.05 $A·g^{-1}$	1000	>87% at 0.05 $A·g^{-1}$	2025	[74]

1T: metallic phase; rGO: reduced graphene oxide; C: C-rate; CNF: carbon nanofiber; GC: graphitic carbon.

on the hydrophobic outer tubes. This structural design effectively mitigated the volume change of the Sn_4P_3 anode, thereby improving the cycling stability. Ji et al. [73] fabricated carbon nanofibers with onion-like structures via low-temperature CVD at 783 K. This distinctive structure is beneficial for the transport and storage of sodium ions. Concurrently, carbon nanofibers (CNFs) prepared at low temperatures not only exhibit a long cycle life, but also offer the advantage of low cost. Similarly, Qiu et al. [71] optimized the CVD synthesis conditions to control both the diameter of carbon nanowires and the thickness of carbon shells on Fe_2P@C (Fig. 3(e)). This core–shell design contributes significantly to realizing a highly conductive electron network, further improving performance. Maulana and Kim [74] developed Fe–Fe_3C@graphitic carbon (GC) composites with exceptional electrochemical performances by incorporating Fe–Fe_3C particles into GC via CVD. Their research showed that Fe–Fe_3C enhanced the sodium storage capacity by promoting the reversible formation and decomposition of the SEI layer, significantly improving battery performance.

In conclusion, the CVD technique, with its ability to produce high-purity and defect-free carbon structures, enables fine control over material morphology and properties. This controllability makes CVD a critical method for fabricating advanced anode materials with exceptional conductivity and cycling stability.

2.1.3. Self-assembly

Self-assembly is relatively straightforward, easy to operate, and generally does not require expensive equipment, leading to low costs (Fig. 4(a)). Consequently, the self-assembly of 3D carbon-based materials is extensively employed, offering two notable advantages. First, by manipulating the reaction conditions and assembling units, 3D carbon materials with tunable pore sizes, porosities, and hierarchical structures can be engineered to optimize performance. Second, varying precursors can yield carbon materials with distinct functionalities by incorporating different elemental compounds for doping purposes (Table 4) [75–79].

When employing self-assembly to fabricate 3D carbon materials, key considerations include precursor selection (ranging from small molecules to polymers) and precise control of reaction parameters such as concentration, stirring, temperature, and time. Elevated temperatures risk pore collapse, whereas lower temperatures may hinder carbonization. Residual impurities from precursors or side reactions often necessitate post-treatments such as calcination or acid washing to ensure material quality.

Generally, self-assembly is known for its mild experimental conditions. Luo et al. [75] electrostatically self-assembled NiS_2 nanoparticles on N-doped graphene (NiS_2/NG) (Fig. 4(b)), resulting in the formation of Ni–N covalent bonds via strong anchoring. The strong coupling between the conducting carbon network and NiS_2 imparted excellent structural integrity, high ionic and electronic conductivity, and strong polysulfide adsorption capacity to the NiS_2/NG composites. Ma et al. [76] utilized a solvent-induced self-assembly approach to fabricate high-nitrogen-containing multicavity mesoporous carbon nanospheres (MCSs) (Fig. 4(c)), which exhibited a reduced SSA. The morphology and SSA of the nanospheres could be precisely controlled by adjusting the reaction time. Furthermore, the incorporation of an amine–phenol bridging

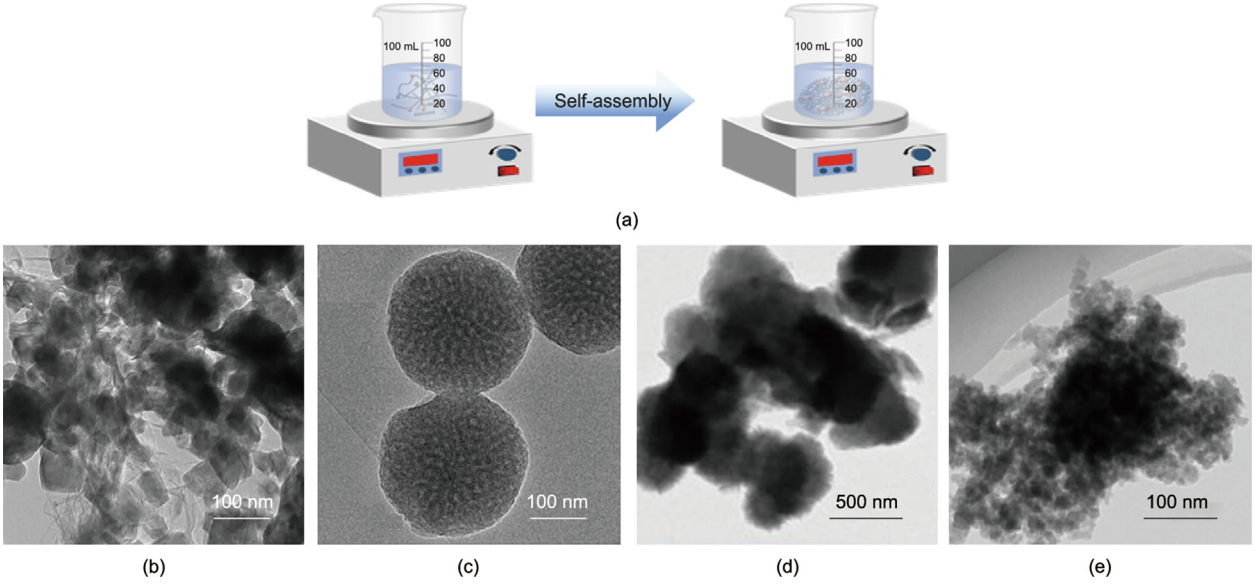


Fig. 4. (a) Schematic of the self-assembly synthesis process. (b–e) TEM images of (b) NiS_2/N-doped graphene (NG), (c) mesoporous carbon nanospheres (MCSs), (d) MoB–MoS_2@C, and (e) Co–2,3,6,7,10,11-hexahydroxytriphenylene (HHTP). (b) Reproduced from Ref. [75] with permission; (c) reproduced from Ref. [76] with permission; (d) reproduced from Ref. [77] with permission; (e) reproduced from Ref. [78] with permission.

Table 4
Electrochemical performances of 3D carbon-host anode materials in SIBs prepared using self-assembly.

Anode	Capacity ($mA{\cdot}h{\cdot}g^{-1}$)	Cycle	Retention	Year	Ref.
NiS_2/NG	722.7 at 0.1 $A{\cdot}g^{-1}$	1200	85% at 0.5 $A{\cdot}g^{-1}$	2024	[75]
MCS	267 at 0.1 $A{\cdot}g^{-1}$	200	>90% at 0.1 $A{\cdot}g^{-1}$	2024	[76]
MoB–MoS_2@C	561 at 0.05 $A{\cdot}g^{-1}$	200	>90% at 0.5 $A{\cdot}g^{-1}$	2024	[77]
N,S-MXene/3DPC	455.2 at 0.2 $A{\cdot}g^{-1}$	1000	73% at 2.0 $A{\cdot}g^{-1}$	2024	[79]
Co–HHTP/G	348 at 0.1 $A{\cdot}g^{-1}$	300	>82% at 0.1 $A{\cdot}g^{-1}$	2024	[78]

3DPC: 3D porous carbon; G: graphene.

structure significantly enhanced the structural integrity and morphological stability of the mesoporous materials, leading to improved long-term performance. Liu et al. [77] developed $Mo_{4/3}B_2T_x$–MoS_2@C composites (Fig. 4(d)) through the synergistic effects of heterogeneous interfaces and Na_2S adsorption/transformation active sites. The 3D spherical structure and heterogeneous interfaces of $Mo_{4/3}B_2T_x$ and MoS_2 improved the intrinsic electrical conductivity and facilitated fast ion diffusion, thereby enhancing electrochemical kinetics. Huang et al. [79] self-assembled N, S co-doped 3D porous carbon (3DPC) with MXene to form N,S-MXene/3DPC composites. This structure, with its high stability and conductivity, reduced MXene aggregation, and N and S doping enhanced the electrochemical performance by increasing the number of active sites for ion storage. Yin et al. [78] synthesized Co–2,3,6,7,10,11-hexahydroxytriphenylene (HHTP) (Fig. 4(e)), a Co-based coordination polymer, on graphene nanosheets via self-assembly. The resulting Co–HHTP/graphene composite exhibited improved electrochemical performance, where graphene mitigates structural stacking, increasing active site accessibility, and enhancing conductivity.

Self-assembly methods offer a simple yet powerful approach for constructing 3D carbon frameworks with tunable porosity and surface functionality. Rational design and precursor selection can further optimize the structural and electrochemical characteristics of anode materials.

2.1.4. Solvothermal method

The solvothermal method is most used for synthesizing 3D carbon-host anode materials because of its low temperature and mild conditions (Fig. 5(a)). This allows for parameter adjustments, such as the solvent type, reaction time, and temperature, to achieve various material morphologies. Ensuring the uniform dispersion of reactants is key, and incorporating compounds with elements such as N and S during synthesis enhances the material properties (Table 5) [48,80–85]. This method is environmentally friendly and uses benign solvents, such as water or alcohols, which produce fewer byproducts.

In solvothermal synthesis, key parameters must be optimized to tailor the material properties. Solvent choice shapes the morphology; alcohols, for instance, aid in carbonization. Temperature governs crystallinity and conductivity, but may damage pores if excessive. Carbon source efficiency affects both carbon yield and porosity, whereas the reaction time must balance completion and over-carbonization. Post-treatments such as washing and calcination are critical for removing residues and enhancing purity and performance.

The composites prepared via partial solvent heating exhibit a flower-like morphology, which results in a high SSA and enhances electrochemical performance. For example, Li et al. [48] synthesized a honeycomb $MoSe_2$/rGO composite through a solvothermal method, where the 3D honeycomb structure not only facilitated electrolyte penetration but also mitigated volume changes. Similarly, Yang et al. [80] synthesized 3D flower-like N-doped carbon (NC)-coated tin nanorods (Sn@NC) (Fig. 5(b)) via solvothermal synthesis. DFT calculations revealed that the surface modification of Sn nanorods with NC markedly enhanced the affinity for Na^+ and facilitated the kinetics of Na^+ diffusion. Chen et al. [81] synthesized NiS–Cu_9S_5/NC ((NiCu)S/NC) (Fig. 5(c)) heterogeneous hollow spheres, in which the NiS/Cu_9S_5 interface served as an active site for Na^+, thereby enhancing electron and ion mobility. Wang et al. [84] coated a $V_{1.11}S_2/V_{1.13}Se_2$ (VSSe) heterogeneous interface with a carbon layer to form VSSe/C. The disulfide/selenide heterointerface in V expanded the interlayer distance, facilitating rapid Na^+ transfer, whereas the multiple defective carbon layers formed during the inhomogeneous process further enhanced ion adsorption and improved the overall electrical conductivity. Xie et al. [82] used a solvothermal method where $SbCl_3$ reacted with ethylene glycol to form a hybrid precursor, which was reduced to carbon-coated Sb after thermal treatment (Sb@carbon microspheres (HCM)@C) (Fig. 5(d)). The carbon coating mitigated volume variations, thereby enhancing the stability and performance of Sb as an anode material. Cheng et al. [85] fabricated binder-free SnS_2 on carbon cloth (CC) using a one-step solvothermal method, incorporating Cu into the SnS_2 lattice to improve the conductivity and Na^+ diffusion (Cu2–SnS_2@CC) (Fig. 5(e)). Liu et al. [83] used a solvothermal method to coat SnO_2 with Zn/Co–ZIFs, followed by thermal treatment to obtain Sn@Zn/Co–N-doped porous carbon (NPC). The carbon coating mitigated volume expansion during cycling and enhanced conductivity.

In summary, solvothermal synthesis provides a flexible and eco-friendly route for designing 3D carbon-host materials with tailored morphologies and compositional features. Careful optimization of the reaction parameters is essential for achieving the desired balance between mechanical robustness and high electrochemical activity.

In addition to the four aforementioned processes for fabricating 3D carbon-host anodes, electrospinning has also been extensively used. For example, Xu et al. [86] constructed a NiSe/C@CNF composite by anchoring NiSe nanoparticles within hollow NC nanofibers via electrospinning and selenization. The 3D interconnected porous carbon framework not only enhanced electron/ion transport but also effectively accommodated the volume expansion of NiSe during cycling. As a result, the electrode delivered an excellent rate capability (300.1 $mA{\cdot}h{\cdot}g^{-1}$ at 5 $A{\cdot}g^{-1}$) and superior long-term cycling stability (85.4% capacity retention after 100 cycles at 0.5 $A{\cdot}g^{-1}$). However, as electrospinning initially fabricates uniform nanowires, which are subsequently combined to obtain the 3D carbon-host anode, it will not be extensively covered in this review.

2.1.5. Comparative analysis of 3D carbon and non-carbon hosts for SIB anodes

To better understand the differences between the 3D carbon and non-carbon hosts for SIB anodes, we provide a direct comparison of their structural features, sodium storage mechanisms, and electrochemical performances (Table 6).

3D carbon-host anodes, including graphene frameworks, carbon nanotubes, and porous carbons, offer excellent electronic conductivity and mechanical flexibility. Their lightweight nature and tunable porous structures facilitate fast electron/ion transport and effectively buffer volume changes during sodiation and desodiation. However, pure carbon frameworks usually suffer from a

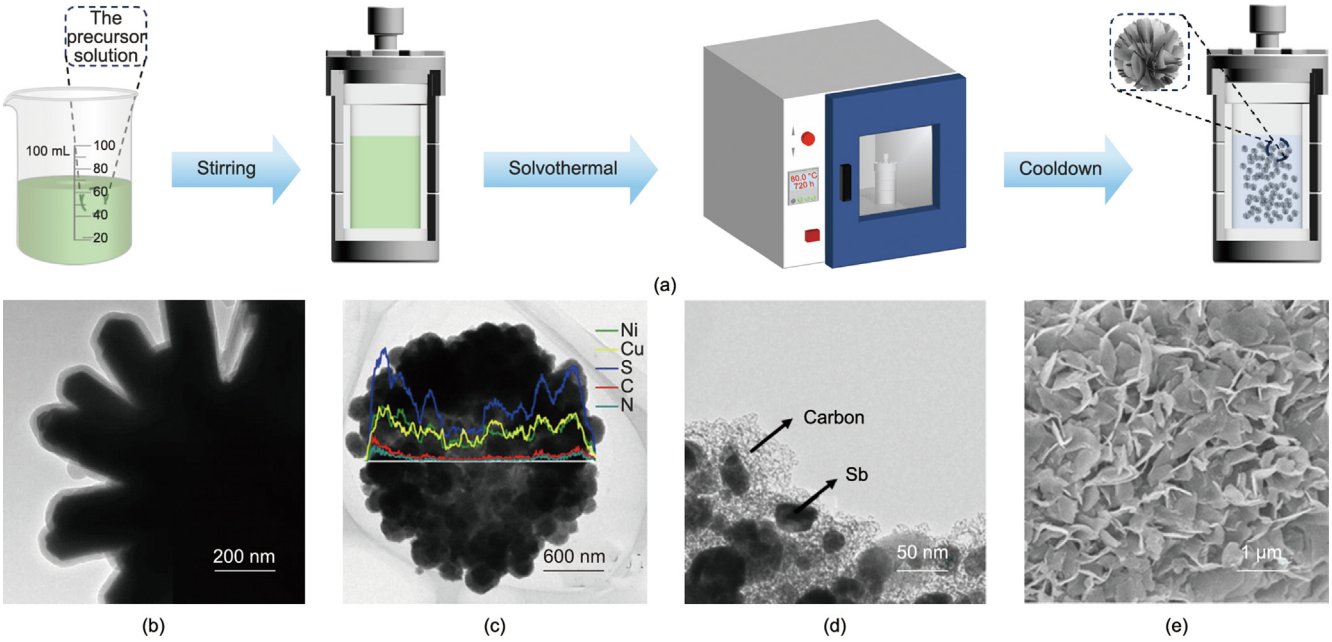


Fig. 5. (a) Schematic of the synthesis process of solvothermal method. (b–d) TEM images of (b) Sn@N-doped carbon (NC), (c) (NiCu)S/NC, and (d) Sb@carbon microspheres (HCM)@C. (e) Scanning electron microscope (SEM) image of Cu2–SnS_2@carbon cloth (CC). (b) Reproduced from Ref. [80] with permission; (c) reproduced from Ref. [81] with permission; (d) reproduced from Ref. [82] with permission; (e) reproduced from Ref. [85] with permission.

Table 5
Electrochemical performances of 3D carbon-host anode materials in SIBs prepared using solvothermal methods.

Anode	Capacity ($mA{\cdot}h{\cdot}g^{-1}$)	Cycle	Retention	Year	Ref.
$MoSe_2$/rGO	449.2 at 0.1 $A{\cdot}g^{-1}$	5900	67% at 8.0 $A{\cdot}g^{-1}$	2024	[48]
Sn@NC	560 at 0.1 $A{\cdot}g^{-1}$	400	>85% at 1.0 $A{\cdot}g^{-1}$	2023	[80]
(NiCu)S/NC	549.3 at 0.5 $A{\cdot}g^{-1}$	1500	81.6% at 4.0 $A{\cdot}g^{-1}$	2023	[81]
VSSe/C	784.9 at 2.0 $A{\cdot}g^{-1}$	1000	>100% at 10.0 $A{\cdot}g^{-1}$	2023	[84]
Sb@HCM@C	332 at 0.1 $A{\cdot}g^{-1}$	100	97.4% at 0.4 $A{\cdot}g^{-1}$	2024	[82]
Cu2–SnS_2@CC	898 at 0.1 $A{\cdot}g^{-1}$	130	68% at 1.6 $A{\cdot}g^{-1}$	2024	[85]
Sn@Zn/Co–NPC	366.13 at 0.1 $A{\cdot}g^{-1}$	200	80% at 0.5 $A{\cdot}g^{-1}$	2025	[83]

VSSe: $V_{1.11}S_2/V_{1.13}Se_2$.

Table 6
Key advantages and limitations of 3D carbon and non-carbon hosts for SIB anodes.

Anode	Advantages	Challenges
3D carbon host	High conductivity, excellent flexibility, stable cycling	Limited capacity, predominantly surface storage
3D non-carbon host	High theoretical capacity, multiple redox reactions	Low conductivity, volume expansion

moderate sodium storage capacity and often require surface modifications or hybridization with active materials to achieve higher capacities.

By contrast, 3D non-carbon-host anodes such as metal foams, MXenes, and transition metal oxides provide higher intrinsic sodium storage capacities and can introduce additional pseudocapacitive behaviors. They also offer strong mechanical support. Nevertheless, their relatively lower conductivities and larger densities compared to those of carbon materials may limit their rate capabilities and practical applications.

2.2. 3D non-carbon-host microstructures

In addition to the widespread use of 3D carbon microstructures as hosts in SIB anode materials, 3D non-carbon microstructures are commonly employed. In these materials, carbon is replaced by oxides [87], sulfides [88–92], phosphates [93], and alloy [94–97], as the primary host, whereas carbon is employed only as a coating or dopant to enhance the conductivity of the material. These SIB anode materials are typically conversion- and alloy-type anodes, offering superior specific capacities compared to intercalation/dein tercalation-type anodes, such as hard-carbon anodes. However, cycling stability remains a challenge and requires further improvement.

2.2.1. 3D-structured oxide anode materials

3D-structured oxides, such as SnO_2 with a theoretical capacity of 1378 $mA{\cdot}h{\cdot}g^{-1}$ (711 $mA{\cdot}h{\cdot}g^{-1}$ from conversion reactions and 667 $mA{\cdot}h{\cdot}g^{-1}$ from alloying reactions) [98], offer high capacities when used as anodes for SIBs (Table 7) [87,99–101]. Their high SSA and porous structure increase the number of Na^+ storage sites and enhance Na^+ diffusion kinetics, thereby improving electrochemical performance. The 3D configuration also accommodates volume changes, enhances cyclic stability, and facilitates stable SEI film formation, thereby minimizing side reactions.

Controlling the size and pore distribution of the 3D oxide particles is crucial during synthesis. Smaller particles shorten the Na-ion diffusion pathways, whereas an optimal pore structure enhances electrolyte infiltration and Na^+ migration. To address the low conductivity of oxide materials, dopants or carbon coatings are essential to create a conductive network that optimizes the electrochemical performance of SIB anodes.

Table 7
Electrochemical performances of 3D-structured oxide anode materials in SIBs.

Anode	Capacity ($mA{\cdot}h{\cdot}g^{-1}$)	Cycle	Retention	Year	Ref.
V_2O_3/C/N	303 at 0.05 $A{\cdot}g^{-1}$	300	107.6% at 0.5 $A{\cdot}g^{-1}$	2024	[87]
VO_x/rGO-5%	336 at 0.1 $A{\cdot}g^{-1}$	100	>80% at 0.1 $A{\cdot}g^{-1}$	2024	[99]
$Co_{2.4}Sn_{0.6}O_4$	576 at 0.08 $A{\cdot}g^{-1}$	100	>75% at 0.08 $A{\cdot}g^{-1}$	2022	[100]
$MnMoO_4$@rGO@g-CN	288 at 0.1 $A{\cdot}g^{-1}$	200	80.7% at 0.2 $A{\cdot}g^{-1}$	2024	[101]

g-CN: graphitic carbon nitride.

Vanadium oxides are widely used as metal oxide anodes. Chen et al. [87] synthesized template-free flower-like V–MOFs, which were subsequently pyrolyzed to obtain V_2O_3/C/N composites (Fig. 6(a)). The pyrolysis temperature plays a significant role in determining the crystallinity of V_2O_3. With increasing temperature, the crystallinity increased, whereas the nitrogen content in the carbon layer was volatilized, resulting in higher graphitization and reduced defects within the carbon structure. The optimal crystallinity and defect density enhanced the number of electrochemically active sites, thereby improving the Na^+ reaction kinetics. Zhang et al. [99] modified vanadium oxide (VO_x) with graphene sheets to obtain VO_x/rGO-5% composites (Fig. 6(b)). In this composite, rGO prevented the agglomeration of VO_x nanorods and enhanced the electron transfer rate within the VO_x matrix. Composite oxide heterostructures consisting of two or more oxides are widely used in energy storage applications. Ali et al. [100] employed a simple precipitation method to modify the crystal structure of $Co_{2+x}Sn_{1-x}O_4$ ($x = 0.2$, 0.4, 0.6, and 0.8), resulting in rod-like $Co_{2.4}Sn_{0.6}O_4$ particles (Fig. 6(c)). These structures provide abundant interfacial sites for stable SEI formation and reduce the occurrence of side reactions. The 3D architecture efficiently accommodates volume changes and enhances cyclic stability. Lee et al. [101] synthesized $MnMoO_4$ using a hydrothermal method and embedded N-doped rGO and graphitic carbon nitride (g-CN) on its surface (Fig. 6(d)) to enhance its conductivity and structural stability.

Overall, 3D-structured oxide anodes leverage their large surface areas and porous networks to enhance Na^+ storage and diffusion kinetics. However, strategies such as conductive coatings and size control must be further refined to overcome their inherent conductivity limitations.

2.2.2. 3D-structured sulfide anode materials

For 3D-structured sulfides, the occurrence of multiple conversion mechanisms in several sulfide materials can significantly enhance their theoretical specific capacities, such as SnS_2 (1136 $mA{\cdot}h{\cdot}g^{-1}$) and Sb_2S_3 (946 $mA{\cdot}h{\cdot}g^{-1}$). Compared to oxides, certain sulfide compounds exhibit superior electrical conductivity, which facilitates Na^+ diffusion and reduces the resistance during charge and discharge cycles, thereby enhancing the rate performance of the battery (Table 8) [89,102–105].

The particle size of sulfide materials significantly affects their surface area, ion diffusion rate, and cycling stability. Therefore, controlling particle size, uniformity, and morphology during preparation is crucial. To enhance conductivity and stability, doping with additional elements or carbon coatings is often necessary, with a focus on the uniform dopant distribution and strong adherence of carbon coatings.

For metal sulfide anodes, mitigating volume change is a crucial challenge. Liu et al. [89] synthesized ultrathin VS_4 nanosheets (Fig. 7(a)) using microwave-assisted synthesis and subsequently controlled the self-assembly of these nanosheets through ligand interactions with NH_4^+, along with the adjustment of the temperature and reaction time, to fabricate hollow nanorod structures. These hollow nanorods, with their unique nanostructures, effectively suppressed volume changes. Similarly, Wang et al. [102] used phytic acid as a phosphorus source to dope PO_4^{3-} into SnS, thereby forming PO_4–SnS (Fig. 7(b)). The introduction of PO_4^{3-} promoted the formation of Sn–O–P bonds, which effectively enhanced electrical conductivity and alleviated the volume change of SnS. Moreover, this doping strategy increased the interlayer spacing, thus promoting a larger Na^+ storage capacity. Additionally, Wang et al. [103] developed a multicomponent metal sulfide heterostructure (SnS/FeS/Fe_3N/NC) (Fig. 7(c)) by incorporating NC nanosheets. These nanostructures feature abundant heterogeneous interfaces, with NC enhancing conductivity and shortening the Na^+ diffusion path, thereby accelerating reaction kinetics. Additionally, Fe_3N promoted the reversible transformation between SnS and FeS during cycling, further improving the electrochemical performance. Xu et al. [104] synthesized a CoS_2/VS_4@NC hollow yolk–shell structure (Fig. 7(d)) using ZIF-67 as a precursor, introducing vanadium via surface etching and ion exchange, followed by sulfidation. The structure provided a high surface area and buffer space to mitigate volume expansion, while the NC layer enhanced conductivity and Na^+ migration. The synergy between CoS_2 and VS_4 accelerated the charge-transfer kinetics. Song et al. [105] converted buckwheat husks into N, S co-doped porous biomass carbon (BC), grew ZIF-67 *in situ*, and applied a dopamine-derived carbon coating. Sulfidation

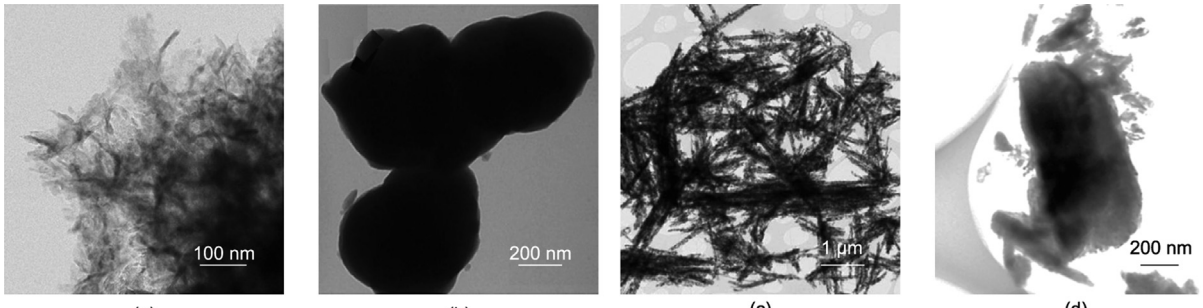


Fig. 6. TEM images of (a) V_2O_3/C/N, (b) VO_x/rGO-5%, (c) $Co_{2.4}Sn_{0.6}O_4$, and (d) $MnMoO_4$@rGO@g-CN. (a) Reproduced from Ref. [87] with permission; (b) reproduced from Ref. [99] with permission; (c) reproduced from Ref. [100] with permission; (d) reproduced from Ref. [101] with permission.

Table 8
Electrochemical performance of the 3D-structured sulfide anode materials of SIBs.

Anode	Capacity ($mA·h·g^{-1}$)	Cycle	Retention	Year	Ref.
VS_4 nanospheres	916.8 at 0.1 $A·g^{-1}$	1000	87.6% at 2.0 $A·g^{-1}$	2022	[89]
PO_4–SnS/NG	476.1 at 0.1 $A·g^{-1}$	300	98.4% at 0.2 $A·g^{-1}$	2022	[102]
SnS/FeS/Fe_3N/NC	796.6 at 0.2 $A·g^{-1}$	600	~60% at 2.0 $A·g^{-1}$	2024	[103]
CoS_2/VS_4@NC	605.8 at 0.1 $A·g^{-1}$	150	>90% at 0.5 $A·g^{-1}$	2024	[104]
C–Co_9S_8/BC	422.56 at 0.1 $A·g^{-1}$	400	~95% at 1.0 $A·g^{-1}$	2025	[105]

BC: biomass carbon.

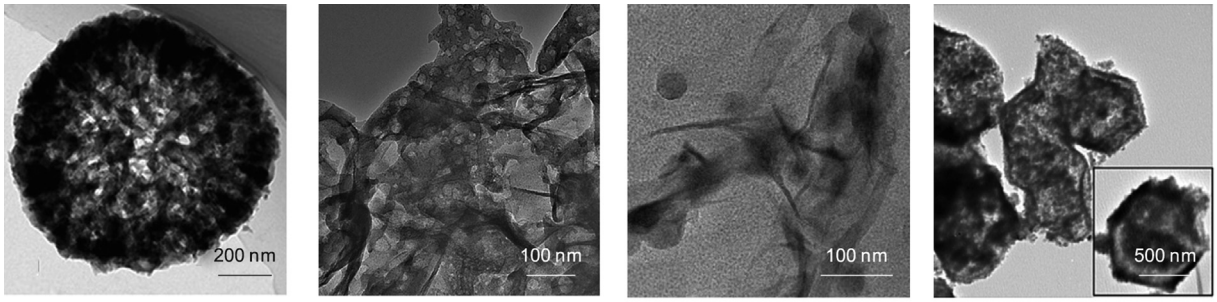


Fig. 7. TEM images of (a) VS_4 nanospheres, (b) PO_4–SnS/NG, (c) SnS/FeS/Fe_3N/NC, and (d) CoS_2/VS_4@NC. (a) Reproduced from Ref. [89] with permission; (b) reproduced from Ref. [102] with permission; (c) reproduced from Ref. [103] with permission; (d) reproduced from Ref. [104] with permission.

produced a three-layer C–Co_9S_8/BC composite. The outer carbon shell inhibited Co_9S_8 dissolution and improved conductivity, the middle layer increased the number of active sites and limited Co_9S_8 aggregation, and the C–S bonds in BC suppressed polysulfide shuttling, maintaining electrode integrity.

Overall, 3D-structured sulfide materials are promising candidates for next-generation SIB anodes owing to their favorable electrical conductivity and high theoretical capacities. However, ensuring phase stability and controlling volume expansion are key areas requiring further investigation.

2.2.3. 3D-structured phosphide anode materials

Phosphides with 3D structures offer superior electrical conductivity compared to sulfides, thereby enhancing electron transfer and reducing polarization in electrochemical reactions. Additionally, many phosphides operate at low voltage platforms in SIBs—such as SbP (0.6–0.8 V), FeP (0.4–0.6 V), and Sn_4P_3 (0.4–0.8 V vs Na/Na^+)—which boosts energy density while minimizing electrolyte decomposition. Their high theoretical capacities further underscore their potential as practical anode materials (Table 9) [106–109].

The phosphate treatment duration and temperature critically influence the morphology and electrochemical performance of phosphate-based materials. Excessive time or high temperatures may lead to particle overgrowth or structural degradation, whereas phosphating often releases toxic gases such as PH_3, necessitating airtight equipment and a controlled atmosphere. Similar to oxides and sulfides, phosphates generally require conductive carbon integration to enhance conductivity and buffer volume changes, making a uniform carbon distribution essential for optimal composite performance.

For metal–phosphide anodes, doping and heterostructures are promising strategies for enhancing performance. Gao et al. [106] prepared self-supported Se-doped Fe_2P arrays ($Fe_2P_{0.8}Se_{0.2}$) (Fig. 8(a)), in which Se doping significantly modulated the charge density distribution, thereby improving the Na adsorption capacity and reducing the diffusion energy barrier for Na^+, which, in turn, enhanced the electrochemical performance. Liu et al. [107] prepared $Fe_{1-x}Co_xP$/NC composites (Fig. 8(b)) via a one-step carbothermal phosphatization method using dopamine-coated Prussian blue analogs as precursors. The Fe–CoP core, encapsulated by a polydopamine-derived NC shell, effectively mitigated the volume change and prevented the aggregation of the active materials. The nanostructured $Fe_{1-x}Co_xP$/NC composite demonstrated an exceptional electrochemical performance, which can be ascribed to the synergistic electronic interactions between the Fe and Co sites. Liu et al. [108] synthesized Co–Cu bimetallic P/C nanocomposites (CoCuP@C) (Fig. 8(c)) via the *in situ* phosphatization and carbonization of polydopamine-coated Co–Cu ZIFs, yielding a core–shell structure with a conductive carbon layer. Cu incorporation increased the conductivity, the carbon shell mitigated aggregation and volume change, and the MOF-derived porosity offered abundant active sites and rapid ion transport. Wu et al. [109] fabricated Sn_xP_y/MXene composites (Fig. 8(d)) by the *in situ* encapsulation of tin phosphide nanoparticles within a conductive MXene framework using hydrothermal treatment and phosphatization [109]. The MXene network buffered volume expansion and prevented Sn_xP_y aggregation, whereas Sn_xP_y provided active sites.

Table 9
Electrochemical performances of 3D-structured phosphide anode materials in SIBs.

Anode	Capacity ($mA·h·g^{-1}$)	Cycle	Retention	Year	Ref.
$Fe_2P_{0.8}Se_{0.2}$	595.1 at 0.1 $A·g^{-1}$	1000	~100% at 1.0 $A·g^{-1}$	2022	[106]
$Fe_{0.17}Co_{0.83}P$/NC	700 at 0.1 $A·g^{-1}$	1000	91.1% at 1.0 $A·g^{-1}$	2024	[107]
CoCuP@C	590 at 0.1 $A·g^{-1}$	200	84.5% at 0.2 $A·g^{-1}$	2024	[108]
Sn_xP_y/MXene	781.4 at 0.05 $A·g^{-1}$	100	72.8% at 1.0 $A·g^{-1}$	2024	[109]

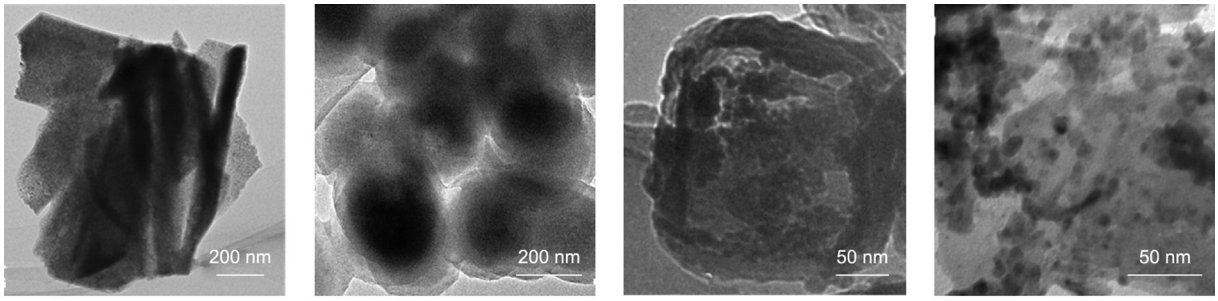


Fig. 8. TEM images of (a) $Fe_2P_{0.8}Se_{0.2}$, (b) $Fe_{0.17}Co_{0.83}P$/NC, (c) CoCuP@C, and (d) Sn_xP_y/Mxene. (a) Reproduced from Ref. [106] with permission; (b) reproduced from Ref. [107] with permission; (c) reproduced from Ref. [108] with permission; (d) reproduced from Ref. [109] with permission.

In summary, 3D phosphide-based anodes demonstrate outstanding conductivity and low operating voltages, contributing to improved energy density and cycling life. Future work should prioritize controlling phosphide phase distribution and interface stability to further improve battery performance.

2.2.4. 3D-structured alloy anode materials

Alloy anodes, such as Sn (847 $mA{\cdot}h{\cdot}g^{-1}$) and Sb (660 $mA{\cdot}h{\cdot}g^{-1}$), offer high theoretical capacities. The established alloying process enables the fine-tuning of the material properties and structure, enhancing the versatility and performance of these anodes (Table 10) [94,95,110–112]. The lower electrochemical stability of alloy anodes makes them prone to powdering during charge–discharge cycles, impacting their conductivity and further reducing their cycle life.

Bai et al. [94] synthesized flower-like $MoTe_2$/C composites (Fig. 9(a)) via chelation, preoxidation, and tellurization. The resulting 3D hierarchical network provided abundant active sites for Na storage, while the *in situ* NC enhanced the ability of the structure to accommodate excess Na^+, offering a larger layer spacing and improved electrical conductivity. As a result, $MoTe_2$/C demonstrated an excellent Coulombic efficiency and cycling stability. Peng et al. [95] successfully synthesized $SbCrSe_3$ heterostructures (Fig. 9(b)) via a solid-state reaction. In this structure, the Sb–Se bonds served as anchors, effectively restricting the migration and aggregation of Sb atoms. Meanwhile, the covalent Cr–Se matrix enhanced the pseudocapacitive behavior, enabling excellent performance under high-rate conditions. Li et al. [110] fabricated a coral-like Sb–Cu nanoarray (Fig. 9(c)) with a dual-gradient distribution (Cu-rich at the top and Sb-rich at the bottom) via template-free electrodeposition. The Cu layer buffered the volume changes and stabilized the interface, whereas the Sb layer delivered a high Na-storage capacity. This gradient design effectively relieved the stress and preserved the structural integrity of the system. Han et al. [111] synthesized a paddy-like Bi–Sb–Cu alloy on Cu foil via template-free pulse-reverse potential electrodeposition. The special structure buffered volume changes and improved electrolyte infiltration while the Cu network increased charge transport. Zheng et al. [112] synthesized Cu–Sb–Sn–Zn–P alloy anodes (Fig. 9(d)) via double-pulse electrodeposition, achieving *in situ* alloying and conductive network formation from a Cu collector. The porous architecture promoted Na^+ transport, whereas Cu incorporation improved the electronic conductivity.

In summary, 3D-structured alloy anodes face mechanical challenges during cycling, despite their remarkable capacity potential. Advanced structural designs and interface engineering are pivotal for realizing their full application potential in practical SIB systems.

3. Conclusion and outlook

In this review, we systematically summarized the structural designs, material classifications, and electrochemical advantages of 3D nanostructured anode materials for SIBs. Special attention was given to 3D carbon-host and non-carbon-host frameworks and the improvement of their storage capacity and cycling stability.

Overall, this review provides a comprehensive overview of the recent advancements in SIBs 3D anode materials, while identifying critical areas for further development and enhancement (Fig. 10) [87,89,94,107].

Achieving commercial 3D anode materials for SIBs requires more than progress at the laboratory scale. Several critical factors must be prioritized for widespread adoption.

3.1. Scalability and cost-effectiveness

The scalability and cost-effectiveness of the fabrication methods remain major obstacles to the commercialization of 3D anode materials. For example, although CVD offers precise control, it is limited by its high cost and low throughput, making it less practical for industrial use. By contrast, solvothermal and freeze-drying-assisted methods are more energy-efficient and scalable but may compromise structural uniformity. To address these challenges, future research should focus on developing low-cost, high-throughput, and environmentally friendly synthetic strategies that retain key structural features. Aligning material design with scalable processing is essential for bridging the gap between laboratory innovation and practical applications in SIB technologies.

Table 10
Electrochemical performances of 3D-structured alloy anode materials in SIBs.

Anode	Capacity ($mA{\cdot}h{\cdot}g^{-1}$)	Cycle	Retention	Year	Ref.
$MoTe_2$/C	282 at 0.1 $A{\cdot}g^{-1}$	3000	>90% at 1.0 $A{\cdot}g^{-1}$	2022	[94]
$SbCrSe_3$	472 at 0.4C	800	96% at 2C	2023	[95]
Sb–Cu	460 at 0.5C	120	89% at 1C	2024	[110]
Bi–Sb–Cu	521.2 at 1C	120	95.5% at 1C	2024	[111]
Cu–Sb–Sn–Zn–P	357.2 at 0.1 $A{\cdot}g^{-1}$	100	99.9% at 0.3 $A{\cdot}g^{-1}$	2025	[112]

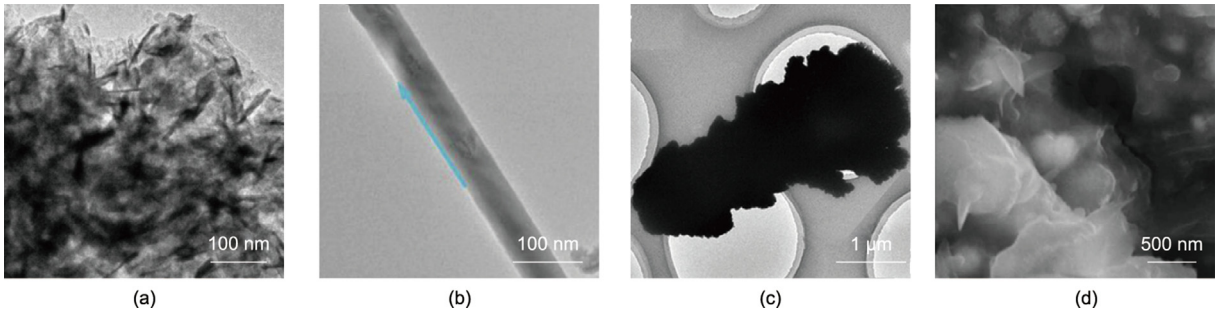


Fig. 9. TEM images of (a) $MoTe_2$/C, (b) $SbCrSe_3$, (c) Sb–Cu, and (d) Cu–Sb–Sn–Zn–P. (a) Reproduced from Ref. [94] with permission; (b) reproduced from Ref. [95] with permission; (c) reproduced from Ref. [110] with permission; (d) reproduced from Ref. [112] with permission.

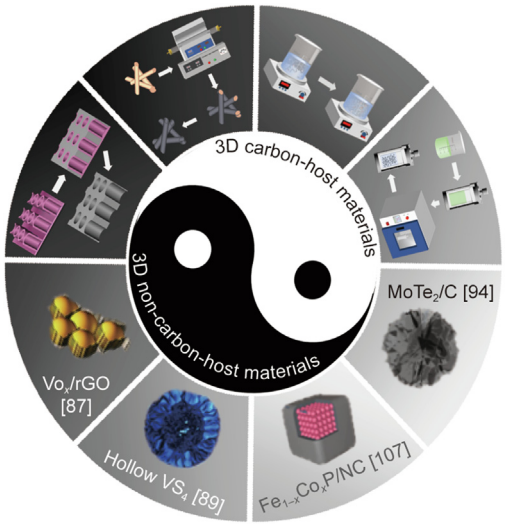


Fig. 10. 3D carbon-host microstructures anode materials obtained using different preparation methods and different 3D non-carbon-host microstructural anode materials for use in SIBs

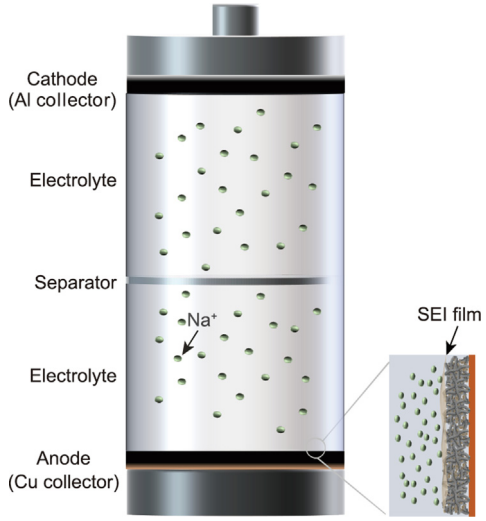


Fig. 11. Schematic of the structure of an SIB and the anode–electrolyte interface.

3.2. Electrode–electrolyte interface optimization

Optimizing the electrode–electrolyte interface is crucial for enhancing the electrochemical performance of 3D anodes. Despite their structural advantages, 3D architectures expose more surface area to electrolytes, leading to side reactions and unstable SEI formation [113,114], which compromise the initial Coulombic efficiency and cycling stability. Functional electrolyte additives such as fluoroethylene carbonate (FEC) can alleviate these issues by forming compact structures [115]. NaF-rich SEI layers can suppress electrolyte decomposition and dendrite formation [116–118] (Fig. 11). Their compatibility with porous 3D frameworks ensures uniform coating of the inner and outer surfaces while maintaining interfacial stability during cycling.

Future designs should focus on electrolyte systems combining additives such as FEC or sodium-difluoro(oxalato)borate (NaDFOB) [119–121] with optimized salt concentrations and solvents tailored to the surface chemistry of 3D anodes. This strategy is essential for achieving high-efficiency, long-cycle-life SIBs.

3.3. Multifunctional integration of structures

Future anode materials must balance multiple attributes such as high capacity, stability, safety, and manufacturability. Enhancing only one property, such as conductivity or mechanical resilience, is insufficient. The development of multifunctional composite structures that combine conductive networks and stress-buffering frameworks is essential for meeting the demands of practical applications.

Heterogeneous structures offer a synergistic enhancement of the properties of similar active materials, significantly boosting electrode performance. When integrated with 3D carbon frameworks, they form conductive networks that effectively buffer volume changes, particularly in alloy-type or modified anodes, thus improving the cycling stability. To overcome the inherent limitations of single 3D architectures and further optimize these systems for energy storage applications, heterointerface engineering has emerged as a promising strategy (such as CoP/CoS_2@NPSC [122] and MnSe@NC@ReS_2 [123]) to enhance the electrochemical properties of electrode materials [124]. The development of heterointerfaces is a highly effective approach for improving internal charge transfer, enhancing structural stability, and accelerating reaction kinetics within electrode materials [124–128]. By introducing heterogeneous phases, these interfaces can spontaneously generate local built-in electric fields that optimize the electronic properties by improving the interface reaction kinetics and reducing ion diffusion barriers (Fig. 12) [128–130]. This phenomenon enables more efficient charge and ion transport, thereby boosting the overall performance of energy storage devices.

3.4. Presodiation techniques

Several targeted strategies can be employed to further exploit the advantages of heterointerfaces. One promising approach is to

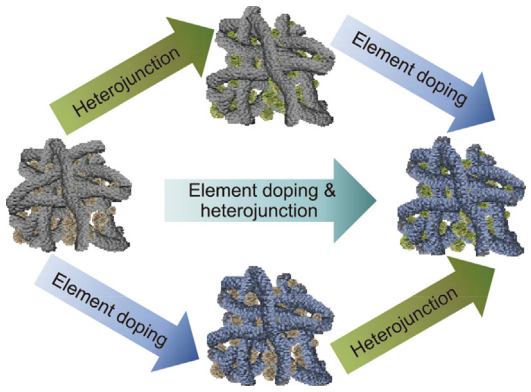


Fig. 12. Schematics illustration of element doping and heterojunction realized on the 3D microstructure anode materials.

create an electric field at an interface. By incorporating specific dopants, it is possible to modulate the electronic environment at the heterointerfaces, thereby fostering a more favorable reaction environment for both charge transfer and ion diffusion. This may be achieved by enhancing the conductivity via C and N incorporation [131], or by enhancing the reaction kinetics through S and N incorporation [131–134]. Moreover, defect engineering, such as creating oxygen vacancies [135–137] or lattice distortions [138–141] at the heterointerface, can further enhance sodium storage by exposing more active sites and reducing the energy barrier for ion transport. When combined, these strategies offer a comprehensive framework for optimizing heterointerface engineering and pushing the boundaries of traditional electrode architectures.

Presodiation techniques should be explored to address the low initial Coulombic efficiency of SIBs. This could mitigate the challenges associated with the initial charge–discharge cycles, ensuring a higher initial efficiency and contributing to long-term durability.

3.5. Standardized testing protocols

A key step in translating 3D anode materials from research to industry is the establishment of standardized evaluation protocols. Currently, inconsistent testing methods make it challenging to compare results across different studies. For industrial applications, it is essential to develop rigorous and reproducible testing standards that reflect real-world operating conditions such as wide temperature ranges, high areal loadings, and long cycle life requirements.

3.6. Overall outlook

Although significant progress has been made in the design of 3D anode materials for SIBs, their commercialization remains hindered by critical technical and economic challenges. Future research should focus on scalable manufacturing techniques, optimization of electrode–electrolyte interfaces, multifunctional structure integration, and practical performance validation. Simultaneously, advancements in high-performance cathode materials [142,143] are essential to fully realize the potential of SIBs and achieve a balanced cell-level performance. By addressing these synergistically aspects, the transition of 3D nanostructured anodes from promising prototypes to reliable commercial products can be accelerated, paving the way for next-generation SIBs with enhanced performance and commercial viability.

HiNa Battery Technology Co., Ltd. has made notable advances in the development of carbon-based anodes for SIBs [144]. Using pyrolyzed anthracite with a high carbon yield (>90%), the company achieved stable capacities around 222 mA·h·g^{-1} and enabled pouch cells with energy densities near 100 W·h·kg^{-1}. To further improve the performance and scalability, HiNa developed soft carbon materials derived from formaldehyde resin (PF) with ethanol as the pore-making agent, reaching capacities of up to 410 mA·h·g^{-1}. These materials offer favorable electrochemical properties, low cost, and compatibility with large-scale production methods. The anode technologies developed by HiNa exhibit low-temperature operation and long cycle life, supporting the commercialization of SIBs for electric mobility and stationary storage applications. Continued optimization of carbon structures and interface stability are key to advancing practical SIB applications.

With the rapid growth in flexible electronics and wearable devices, the demand for stable SIBs has increased (Fig. 13). This progress calls for a shift in traditional battery designs, focusing on inherently flexible 3D structures that surpass current limitations. Research must explore new ways to integrate advanced polymer matrices with biomimetic structures, balancing mechanical durability and electrochemical performance.

Flexible SIBs are critical for next-generation energy storage devices, particularly for wearable electronics, portable devices, and flexible energy solutions. As the need for lightweight, bendable, and durable batteries increases, flexible SIBs have become reliable power sources for a variety of devices, ranging from fitness trackers and smartwatches to foldable electronics. These batteries can be seamlessly integrated into fabrics and flexible circuits, making them ideal for wearable technologies and flexible consumer devices.

Flexible SIBs hold great promise in the fields of robotics, healthcare, and renewable energy. In robotics, they can provide lightweight and efficient power to soft robots that require flexibility in dynamic movements. In healthcare, flexible SIBs can be embedded in medical wearables for continuous health monitoring. Renewable energy can be integrated into flexible solar panels or energy-harvesting systems to provide portable and adaptable storage solutions.

In summary, flexible SIBs are expected to play a key role in future energy storage systems. As materials and engineering advancements continue, they will become essential components of wearable electronics, smart devices, and emerging technologies that require lightweight, reliable, and flexible power sources.

Overall, although SIBs have made significant advancements and are beginning to enter the commercialization phase, we believe that their commercial potential has not yet been fully realized. Therefore, in-depth research into the aforementioned limitations of these systems is essential to accelerate the development of SIBs.

CRediT authorship contribution statement

Honglin Ren: Writing – original draft, Investigation, Conceptualization. **Zihan Zhou:** Writing – original draft, Investigation. **Feng Wu:** Writing – review & editing, Supervision. **Siyuan Liu:** Investigation. **Guoqiang Tan:** Writing – review & editing, Supervision. **Xinyi Tan:** Writing – review & editing, Writing – original draft, Supervision, Investigation, Funding acquisition, Conceptualization.

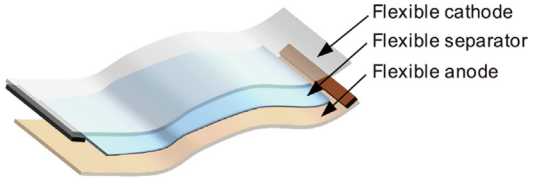


Fig. 13. Schematic of the structure of a flexible battery.

Declaration of competing interest

The authors declare that they have no known competing financial interests or personal relationships that could have appeared to influence the work reported in this paper.

Acknowledgments

This work was supported by National Major Science and Technology Projects of China (2026ZD0622001) and National Nature Science Foundation of China (U24B20201).

References

[1] York R. Do alternative energy sources displace fossil fuels? Nat Clim Chang 2012;2(6):441–3.
[2] Zhao S, Yan K, Zhang J, Sun B, Wang G. Reaction mechanisms of layered lithium-rich cathode materials for high-energy lithium-ion batteries. Angew Chem Int Ed 2021;60(5):2208–20.
[3] Zhao Q, Huang Y, Hu X. A Si/C nanocomposite anode by ball milling for highly reversible sodium storage. Electrochem Commun 2016;70:8–12.
[4] Zhao C, Lu Y, Li Y, Jiang L, Rong X, Hu YS, et al. Novel methods for sodium-ion battery materials. Small Methods 2017;1(5):1600063.
[5] Oszajca MF, Bodnarchuk MI, Kovalenko MV. Precisely engineered colloidal nanoparticles and nanocrystals for Li-ion and Na-ion batteries: model systems or practical solutions? Chem Mater 2014;26(19):5422–32.
[6] Liu Y, Liu X, Wang T, Fan LZ, Jiao L. Research and application progress on key materials for sodium-ion batteries. Sustain Energy Fuels 2017;1(5):986–1006.
[7] Dahbi M, Yabuuchi N, Kubota K, Tokiwa K, Komaba S. Negative electrodes for Na-ion batteries. Phys Chem Chem Phys 2014;16(29):15007–28.
[8] Chen L, Fiore M, Wang JE, Ruffo R, Kim DK, Longoni G. Readiness level of sodium-ion battery technology: a materials review. Adv Sustain Syst 2018;2(3):1700153.
[9] Yang C, Xin S, Mai L, You Y. Materials design for high-safety sodium-ion battery. Adv Energy Mater 2021;11(2):2000974.
[10] Bauer A, Song J, Vail S, Pan W, Barker J, Lu Y. The scale-up and commercialization of nonaqueous Na-ion battery technologies. Adv Energy Mater 2018;8(17):1702869.
[11] Vaalma C, Buchholz D, Weil M, Passerini S. A cost and resource analysis of sodium-ion batteries. Nat Rev Mater 2018;3:18013.
[12] Tan H, Chen D, Rui X, Yu Y. Peering into alloy anodes for sodium-ion batteries: current trends, challenges, and opportunities. Adv Funct Mater 2019;29(14):1808745.
[13] Zhang Y, Chen L, Meng Y, Xie J, Guo Y, Xiao D. Lithium and sodium storage in highly ordered mesoporous nitrogen-doped carbons derived from honey. J Power Sources 2016;335:20–30.
[14] Li D, Chen L, Chen L, Sun Q, Zhu M, Zhang Y, et al. Potassium gluconate-derived N/S Co-doped carbon nanosheets as superior electrode materials for supercapacitors and sodium-ion batteries. J Power Sources 2019;414:308–16.
[15] Li Z, Chen Y, Jian Z, Jiang H, Razink JJ, Stickle WF, et al. Defective hard carbon anode for Na-ion batteries. Chem Mater 2018;30(14):4536–42.
[16] Stevens DA, Dahn JR. The mechanisms of lithium and sodium insertion in carbon materials. J Electrochem Soc 2001;148(8):A803–11.
[17] Au H, Alptekin H, Jensen ACS, Olsson E, O'Keefe CA, Smith T, et al. A revised mechanistic model for sodium insertion in hard carbons. Energy Environ Sci 2020;13(10):3469–79.
[18] Wang Z, Feng X, Bai Y, Yang H, Dong R, Wang X, et al. Probing the energy storage mechanism of quasi-metallic Na in hard carbon for sodium-ion batteries. Adv Energy Mater 2021;11(11):2003854.
[19] Wu C, Dou SX, Yu Y. The state and challenges of anode materials based on conversion reactions for sodium storage. Small 2018;14(22):1703671.
[20] Lao M, Zhang Y, Luo W, Yan Q, Sun W, Dou SX. Alloy-based anode materials toward advanced sodium-ion batteries. Adv Mater 2017;29(48):1700622.
[21] Wang JW, Liu XH, Mao SX, Huang JY. Microstructural evolution of tin nanoparticles during *in situ* sodium insertion and extraction. Nano Lett 2012;12(11):5897–902.
[22] Ellis LD, Hatchard TD, Obrovac MN. Reversible insertion of sodium in tin. J Electrochem Soc 2012;159(11):A1801–5.
[23] Wu L, Lu H, Xiao L, Ai X, Yang H, Cao Y. Electrochemical properties and morphological evolution of pitaya-like Sb@C microspheres as high-performance anode for sodium ion batteries. J Mater Chem A 2015;3(10):5708–13.
[24] Qian J, Chen Y, Wu L, Cao Y, Ai X, Yang H. High capacity Na-storage and superior cyclability of nanocomposite Sb/C anode for Na-ion batteries. Chem Commun 2012;48(56):7070–2.
[25] Jung SC, Kim HJ, Kang YJ, Han YK. Advantages of Ge anode for Na-ion batteries: Ge vs. SI and Sn. J Alloys Compd 2016;688(Pt B):158–63.
[26] Kohandehghan A, Cui K, Kupsta M, Ding J, Memarzadeh Lotfabad E, Kalisvaart WP, et al. Activation with Li enables facile sodium storage in germanium. Nano Lett 2014;14(10):5873–82.
[27] Fu Y, Wei Q, Zhang G, Sun S. Advanced phosphorus-based materials for lithium/sodium-ion batteries: recent developments and future perspectives. Adv Energy Mater 2018;8(13):1703058.
[28] Kim Y, Park Y, Choi A, Choi NS, Kim J, Lee J, et al. An amorphous red phosphorus/carbon composite as a promising anode material for sodium ion batteries. Adv Mater 2013;25(22):3045–9.
[29] Ellis LD, Wilkes BN, Hatchard TD, Obrovac MN. *In situ* XRD study of silicon, lead and bismuth negative electrodes in nonaqueous sodium cells. J Electrochem Soc 2014;161(3):A416–21.
[30] Mortazavi M, Ye Q, Birbilis N, Medhekar NV. High capacity group-15 alloy anodes for Na-ion batteries: electrochemical and mechanical insights. J Power Sources 2015;285:29–36.
[31] Chevrier VL, Ceder G. Challenges for Na-ion negative electrodes. J Electrochem Soc 2011;158(9):A1011–4.
[32] Luo W, Shen F, Bommier C, Zhu H, Ji X, Hu L. Na-ion battery anodes: materials and electrochemistry. Acc Chem Res 2016;49(2):231–40.
[33] Winkler V, Kilibarda G, Schlabach S, Szabó DV, Hanemann T, Bruns M. Surface analytical study regarding the solid electrolyte interphase composition of nanoparticulate SnO_2 anodes for Li-ion batteries. J Phys Chem C 2016;120(43):24706–14.
[34] Ji L, Gu M, Shao Y, Li X, Engelhard MH, Arey BW, et al. Controlling SEI formation on SnSb-porous carbon nanofibers for improved Na ion storage. Adv Mater 2014;26(18):2901–8.
[35] Bodenes L, Darwiche A, Monconduit L, Martinez H. The solid electrolyte interphase a key parameter of the high performance of Sb in sodium-ion batteries: comparative X-ray photoelectron spectroscopy study of Sb/Na-ion and Sb/Li-ion batteries. J Power Sources 2015;273:14–24.
[36] Komaba S, Ishikawa T, Yabuuchi N, Murata W, Ito A, Ohsawa Y. Fluorinated ethylene carbonate as electrolyte additive for rechargeable Na batteries. ACS Appl Mater Interfaces 2011;3(11):4165–8.
[37] Darwiche A, Bodenes L, Madec L, Monconduit L, Martinez H. Impact of the salts and solvents on the SEI formation in Sb/Na batteries: an XPS analysis. Electrochim Acta 2016;207:284–92.
[38] Xu Y, Zhu Y, Liu Y, Wang C. Electrochemical performance of porous carbon/tin composite anodes for sodium-ion and lithium-ion batteries. Adv Energy Mater 2013;3(1):128–33.
[39] Zhang Z, Zhao X, Li J. SnSe/carbon nanocomposite synthesized by high energy ball milling as an anode material for sodium-ion and lithium-ion batteries. Electrochim Acta 2015;176:1296–301.
[40] Zhang Y, Wang H, Luo Z, Tan HT, Li B, Sun S, et al. An air-stable densely packed phosphorene–graphene composite toward advanced lithium storage properties. Adv Energy Mater 2016;6(12):1600453.
[41] Lim CH, Huang TY, Shao PS, Chien JH, Weng YT, Huang HF, et al. Experimental study on sodiation of amorphous silicon for use as sodium-ion battery anode. Electrochim Acta 2016;211:265–72.
[42] Chu C, Li R, Cai F, Bai Z, Wang Y, Xu X, et al. Recent advanced skeletons in sodium metal anodes. Energy Environ Sci 2021;14(8):4318–40.
[43] Xu E, Li P, Quan J, Zhu H, Wang L, Chang Y, et al. Dimensional gradient structure of $CoSe_2$@CNTs–MXene anode assisted by ether for high-capacity, stable sodium storage. Nano-Micro Lett 2021;13(1):40.
[44] Yue L, Wu D, Wu Z, Zhao W, Wang D, Zhong B, et al. A MnS/FeS_2 heterostructure with a high degree of lattice matching anchored into carbon skeleton for ultra-stable sodium-ion storage. J Mater Chem A 2021;9(42):24024–35.
[45] Qin J, Wang T, Liu D, Liu E, Zhao N, Shi C, et al. A top-down strategy toward SnSb in-plane nanoconfined 3D N-doped porous graphene composite microspheres for high performance Na-ion battery anode. Adv Mater 2018;30(9):1704670.
[46] Hu X, Li Y, Zeng G, Jia J, Zhan H, Wen Z. Three-dimensional network architecture with hybrid nanocarbon composites supporting few-layer MoS_2 for lithium and sodium storage. ACS Nano 2018;12(2):1592–602.
[47] Han J, Kong D, Lv W, Tang DM, Han D, Zhang C, et al. Caging tin oxide in three-dimensional graphene networks for superior volumetric lithium storage. Nat Commun 2018;9:402.
[48] Li Z, Yu L, Tao X, Li Y, Zhang L, He X, et al. Honeycomb-structured $MoSe_2$/rGO composites as high-performance anode materials for sodium-ion batteries. Small 2024;20(6):2304124.
[49] Zhao D, Zhang Z, Ren J, Xu Y, Xu X, Zhou J, et al. Fe_2VO_4 nanoparticles on rGO as anode material for high-rate and durable lithium and sodium ion batteries. Chem Eng J 2023;451(Pt 3):138882.
[50] Liang M, Ma L, Chen B, Liu E, Shi C, He C, et al. Two birds with one stone: a NaCl-assisted strategy toward $MoTe_2$ nanosheets nanoconfined in 3D porous carbon network for sodium-ion battery anode. Energy Storage Mater 2022;47:591–601.
[51] Liu Z, Sun H, Wang X, Gu ZY, Xu C, Li H, et al. Tetrafunctional template-assisted strategy to preciously construct co-doped Sb@C nanofiber with longitudinal tunnels for ultralong-life and high-rate sodium storage. Energy Storage Mater 2022;48:90–100.
[52] Liang M, Xie H, Liu E, Shi C, He C, Zhao N. Ultrafine Fe_3N nanocrystals coupled with N doped 3D porous carbon networks induced atomically dispersed Fe for superior sodium ion storage. Carbon 2022;196:795–806.
[53] Yang F, Wang S, Guan J, Shao L, Shi X, Cai J, et al. Hierarchical MoS_2–NiS nanosheet-based nanotubes@N-doped carbon coupled with ether-based electrolytes towards high-performance Na-ion batteries. J Mater Chem A 2021;9(47):27072–83.

[54] Tan X, Mo R, Xu J, Li X, Yin Q, Shen L, et al. High performance sodium ion anodes based on Sn_4P_3 encapsulated within amphiphilic graphene tubes. Adv Energy Mater 2022;12(2):2102345.
[55] Mo R, Tan X, Li F, Tao R, Xu J, Kong D, et al. Tin-graphene tubes as anodes for lithium-ion batteries with high volumetric and gravimetric energy densities. Nat Commun 2020;11:1374.
[56] Jiang Y, Xie M, Wu F, Ye Z, Zhang Y, Wang Z, et al. Cobalt selenide hollow polyhedron encapsulated in graphene for high-performance lithium/sodium storage. Small 2021;17(40):2102893.
[57] Ma M, Wang H, Xiong L, Huang S, Li X, Du X. Self-assembled homogeneous SiOC@C/graphene with three-dimensional lamellar structure enabling improved capacity and rate performances for lithium ion storage. Carbon 2022;186:273–81.
[58] Xia Y, Yang T, Wang Z, Mao T, Hong Z, Han J, et al. Van der Waals forces between S and P ions at the CoP–C@MoS_2/C heterointerface with enhanced lithium/sodium storage. Adv Funct Mater 2023;33(35):2302830.
[59] Yu M, Sun M, Zhu L, Luo Z, Deng G, Zou C, et al. Double-shell and hierarchical porous nitrogen-doped carbon nanocages as superior anode material for advanced sodium-ion batteries. J Energy Storage 2024;86(Pt A):111211.
[60] Ou H, Li P, Jiang C, Liu Y, Luo Y, Xing Z, et al. Synergistic enhancement of Ni_2P anode for high lithium/sodium storage by N, P, S triply-doping and soft template-assisted strategy. J Colloid Interface Sci 2025;678(Pt A):365–77.
[61] Wen C, Huang M, Feng C, Kong N, Hou K, Xie R, et al. Construction of microporous structure in hard carbon via adjustable Zn salt templates for high-performance sodium-ion batteries. Carbon 2024;230:119702.
[62] Gao F, Zhang D, Zhang H, Gao C, Huang G, Zhang Z, et al. Liquid bath-assisted combustion activation preparation of nitrogen/sulfur-doped porous carbon for sodium-ion battery applications. Carbon 2024;229:119481.
[63] Lu Z, Zhang P, Li D, Yin F, Weng J, Cong H. MOF-derived defect-rich $CoTe_2$ confined in graphene aerogel for superior sodium/potassium storage with ultralong lifespan. Chem Eng J 2025;506:159896.
[64] Zhang D, Huang G, Zhang H, Zhang Z, Liu Y, Gao F, et al. Soft template-induced self-assembly strategy for sustainable production of porous carbon spheres as anode towards advanced sodium-ion batteries. Chem Eng J 2024;495:153646.
[65] Dong Y, Li Y, Shi H, Qin J, Zheng S, He R, et al. Graphene encapsulated iron nitrides confined in 3D carbon nanosheet frameworks for high-rate lithium ion batteries. Carbon 2020;159:213–20.
[66] Zhou J, Qin J, Zhang X, Shi C, Liu E, Li J, et al. 2D space-confined synthesis of few-layer MoS_2 anchored on carbon nanosheet for lithium-ion battery anode. ACS Nano 2015;9(4):3837–48.
[67] Qin J, He C, Zhao N, Wang Z, Shi C, Liu EZ, et al. Graphene networks anchored with Sn@graphene as lithium ion battery anode. ACS Nano 2014;8(2):1728–38.
[68] Li X, Zheng S, Jin L, Li Y, Geng P, Xue H, et al. Metal–organic framework-derived carbons for battery applications. Adv Energy Mater 2018;8(23):1800716.
[69] Chen X, Xu Z, Liu Y, Li G, Zhao S, Zhang X, et al. Towards a widely operate temperature sodium-ion battery via a new zinc phosphate anode material. Chem Eng J 2025;506:160014.
[70] Zhou Z, Wang S, Wen B, Xiao J, Yang G, Ding S. Waste tire-derived graphene modified carbon as anodes for sodium-ion batteries. Mater Today Sustain 2024;27:100874.
[71] Qiu Y, Fu F, Hu M, Shen PK, Zhu J. Tailored chemically bonded metal phosphide@carbon nanowire arrays on foam metal as an all-in-one anode for ultrahigh-area-capacity sodium-ion batteries. Chem Eng J 2023;454(Pt 3):140402.
[72] Li Z, Zheng J, Xiao M, Jiang H, Wang L, Song H, et al. Three-dimensional 1T-SnS_2 wrapped with graphene for sodium-ion battery anodes with highly reversible sodiation/desodiation. Scr Mater 2022;211:114500.
[73] Ji S, Wang L, Fan X, Wang M, Li P, Liu L, et al. Electrochemical properties of carbon nanofibers as anode for rechargeable sodium-ion batteries. Diamond Relat Mater 2025;152:111923.
[74] Maulana AY, Kim J. Investigation of solid electrolyte interphase regarding extra capacity in Fe–Fe_3C as a superior sodium-ion anode material. Small 2025;21(6):2410174.
[75] Luo S, Shang J, Xu Y, Cheng H, Zhang L, Tang Y. Stabilizing NiS_2 on conductive component via electrostatic self-assembly and covalent bond strategy for promoting sodium storage. Adv Funct Mater 2024;34(39):2403166.
[76] Ma W, Huang G, Yu L, Miao X, An X, Zhang J, et al. Synthesis of multi-cavity mesoporous carbon nanospheres through solvent-induced self-assembly: anode material for sodium-ion batteries with long-term cycle stability. J Colloid Interface Sci 2024;654(Pt B):1447–57.
[77] Liu G, Yuan W, Zhao Z, Li J, Wu N, Guo D, et al. $Mo_{4/3}B_2T_x$ induced hierarchical structure and rapid reaction dynamics in MoS_2 anode for superior sodium storage. Chem Eng J 2024;493:152576.
[78] Yin X, Liu Y, Xie Z, Zhao F, Zuo P, Wang N, et al. Boosting potassium and sodium-ion storage performance by *in-situ* self-assembly of a Co-based π–d conjugated coordination polymer on graphene nanosheets. J Energy Storage 2024;91:112111.
[79] Huang Y, Xu Y, Wang J, Bao S, Zhang Y, Yin Y, et al. Self-assembly of N,S-MXene/3DPC heterostructure with multiple charge transfer channels for high-performance supercapacitors and sodium-ion batteries. J Power Sources 2024;601:234312.
[80] Yang J, Guo X, Gao H, Wang T, Liu Z, Yang Q, et al. A high-performance alloy-based anode enabled by surface and interface engineering for wide-temperature sodium-ion batteries. Adv Energy Mater 2023;13(29):2300351.
[81] Chen H, Lv P, Tian P, Cao S, Yuan S, Liu Q. Hollow sphere of heterojunction (NiCu)S/NC as advanced anode for sodium-ion battery. J Energy Chem 2023;82:248–58.
[82] Xie X, Liang Q, Huang S. Solvothermal-induced synthesis of *in-situ* carbon-coated antimony nanoparticles as an anode material for sodium-ion batteries. ChemistrySelect 2024;9(3):e202305056.
[83] Liu X, Li M, Shi C, Wang J, Yao S. Sn@Zn/Co-NPC as anode materials for sodium-ion batteries via the solvothermal method. J Electron Mater 2025;54(1):634–46.
[84] Wang J, Cui J, Li Z, Zhang D, Sun H, Wang H, et al. Polysulfide-derived anion heterogeneous interfaces engineering to facilitate high-efficiency sodium ion storage. Chem Eng J 2023;464:142764.
[85] Cheng TM, Lin KH, Kongvarhodom C, Chen HM, Husain S, Yougbaré S, et al. Design of novel Cu-doped SnS_2 on carbon cloth as a binder-free anode to improve high-rate performance of sodium ion battery. New J Chem 2024;48(20):9163–71.
[86] Xu LJ, Wang XJ, Tang GY, Zhu BC, Yu JG, Zhang LY, et al. NiSe nanoparticles anchored on hollow carbon nanofibers with enhanced rate capability and prolonged cycling durability for sodium-ion batteries. Rare Met 2025;44(1):185–94.
[87] Chen H, Hu H, Shen T, Li H, Zhou H. Metal–organic frameworks derived flower-like V_2O_3/C/N for high-performance sodium storage. Chem Eng J 2024;487:150316.
[88] Cheng S, Yao K, Zheng K, Li Q, Chen D, Jiang Y, et al. Self-assembled VS_4 hierarchitectures with enhanced capacity and stability for sodium storage. Energy Environ Mater 2022;5(2):592–8.
[89] Liu B, Wang L, Zhu Y, Peng H, Du C, Yang X, et al. Ammonium-modified synthesis of vanadium sulfide nanosheet assemblies toward high sodium storage. ACS Nano 2022;16(8):12900–9.
[90] Wang Y, Liu J, Chen X, Kang B, Wang HE, Xiong P, et al. Structural engineering of tin sulfides anchored on nitrogen/phosphorus dual-doped carbon nanofibres in sodium/potassium-ion batteries. Carbon 2022;189:46–56.
[91] Yue X, Wang J, Xie Z, He Y, Liu Z, Liu C, et al. Controllable synthesis of novel orderly layered $VMoS_2$ anode materials with super electrochemical performance for sodium-ion batteries. ACS Appl Mater Interfaces 2021;13(22):26046–54.
[92] Zhang Y, Li J, Ma L, Li H, Xu X, Liu X, et al. Insights into the storage mechanism of 3D nanoflower-like V_3S_4 anode in sodium-ion batteries. Chem Eng J 2022;427:130936.
[93] Gong H, Du T, Zhou L, Liu L, Wang Y, Jia H, et al. 3D substrate self-sacrifice Ni_2P integrated anode for high-performance sodium-ion battery. J Alloys Compd 2022;928:167108.
[94] Bai J, Zhang L, Li S, Ren H, Liu Y, Guo S. Self-assembled $MoTe_2$ hierarchical nanoflowers with carbon coating as anode material for excellent sodium storage performance. Chem Eng J 2023;452(Pt 1):139111.
[95] Peng B, Xu S, Lv Z, Zhang S, Gao Y, Lin T, et al. Toward extremely fast charging through boosting intercalative redox pseudocapacitance: a $SbCrSe_3$ anode for large and fast sodium storage. Adv Energy Mater 2023;13(2):2203187.
[96] Pu B, Liu Y, Bai J, Chu X, Zhou X, Qing Y, et al. Iodine-ion-assisted galvanic replacement synthesis of bismuth nanotubes for ultrafast and ultrastable sodium storage. ACS Nano 2022;16(11):18746–56.
[97] Xu M, Ma Y, Liu R, Xiao H, Chen L, Zhang Z, et al. Constructing electron transport channels in $FeSe_2$ microspheres by a facile strategy for superior long-life and ultrafast sodium-ion storage. Chem Eng J 2023;467:143382.
[98] Ying H, Han WQ. Metallic Sn-based anode materials: application in high-performance lithium-ion and sodium-ion batteries. Adv Sci 2017;4(11):1700298.
[99] Zhang Q, Liao S, Yu H, Liu B, Jiang K, Gao Y, et al. Surface modification boosting amorphous vanadium oxides anode toward stable and rapid sodium ion storage. J Energy Storage 2024;78:110211.
[100] Ali G, Islam M, Bhange DS, Jung YH, Ge M, Chu YS, et al. Self-standing $Co_{2.4}Sn_{0.6}O_4$ nano rods as high performance anode materials for sodium-ion battery and investigation on its reaction mechanism. Chem Eng J 2022;439:135791.
[101] Lee SJ, Moorthy M, Park S, Lee YS. Enhanced nitrogen-doped reduced graphene oxide-embedded $MnMoO_4$ as high-capacity and stable anode for sodium-ion batteries. J Ind Eng Chem 2024;131:199–207.
[102] Wang Y, Li H, Chen S, Zhai B, Di S, Gao G, et al. An ultralong-life SnS-based anode through phosphate-induced structural regulation for high-performance sodium ion batteries. Sci Bull 2022;67(20):2085–95.
[103] Wang S, Xie S, Zhang M, Jiang Y, Luo H, Tang J, et al. Interface engineering of metal sulfides-based composites enables high-performance anode materials for sodium-ion batteries. J Colloid Interface Sci 2024;663:387–95.
[104] Xu F, Li S, Jing S, Peng X, Yuan L, Lu S, et al. Cobalt–vanadium sulfide yolk–shell nanocages from surface etching and ion-exchange of ZIF-67 for ultra-high rate-capability sodium ion battery. J Colloid Interface Sci 2024;660:907–15.
[105] Song JX, Deng DR, Cai SL, Huang H, Li GF, Zeng Y, et al. Effective protection for cobalt sulfide constructed using a three-layer core–shell structure in biomass carbon for sodium ion batteries. J Power Sources 2025;629:236056.
[106] Gao L, Liu Y, Hao Y, Zheng Z, Kong S, Zhang L, et al. Self supported selenium doped Fe_2P hierarchical microsphere arrays enabling high performance sodium ion batteries. J Alloys Compd 2022;918:165647.

[107] Liu S, Qin Z, Guo J, Guo S, Zhou Z, Shi Q, et al. Iron–cobalt phosphide/nitrogen-doped carbon composite derived from Prussian blue analogues as anode materials for sodium-ion batteries. J Energy Storage 2024;98(Pt A):113131.
[108] Liu S, Ren L, Tian Y, Shi Q, Tong J, Xing X. Cobalt–copper bimetallic phosphide/carbon nanocomposites derived from metal–organic frameworks for sodium-ion batteries. ACS Appl Nano Mater 2024;7(14):16639–48.
[109] Wu CF, Kubendhiran S, Chung RJ, Kongvarhodom C, Husain S, Yougbaré S, et al. Novel *in-situ* encapsulation of tin phosphide particles in MXene conductive networks as anode materials of the durable sodium-ion battery. J Colloid Interface Sci 2024;675:792–805.
[110] Li X, Li C, Zhang X, Sun J, Liu X, Song K, et al. Dual-gradient concentration distribution in Sb–Cu alloy nanoarrays for robust sodium-ion storage. Angew Chem Int Ed 2024;63(45):e202412533.
[111] Han X, Zheng X, You J, Wang J, Hou J, Zhu Z, et al. Novel paddy-like Bi–Sb–Cu alloy fabricated via pulse reverse potential electrodeposition enabling high-performance sodium-ion batteries. Chem Eng J 2024;490:151975.
[112] Zheng X, Zhu Z, Wang J, Hou J, Zhang H, Shen H, et al. Binder-free Cu–Sb–Sn–Zn–P alloys as high-efficiency anodes for sodium-ion batteries via double-pulse electrodeposition. J Alloys Compd 2025;1010:177048.
[113] Mogensen R, Brandell D, Younesi R. Solubility of the solid electrolyte interphase (SEI) in sodium ion batteries. ACS Energy Lett 2016;1(6):1173–8.
[114] Bommier C, Ji X. Electrolytes, SEI formation, and binders: a review of nonelectrode factors for sodium-ion battery anodes. Small 2018;14(16):1703576.
[115] Wang E, Wan J, Guo YJ, Zhang Q, He WH, Zhang CH, et al. Mitigating electron leakage of solid electrolyte interface for stable sodium-ion batteries. Angew Chem Int Ed 2023;62(4):e202216354.
[116] Bouibes A, Sakaki N, Nagaoka M. Microscopic analysis of the mechanical stability of an SEI layer structure depending on the FEC additive concentration in Na-ion batteries: maximum appearance in Vickers hardness at lower FEC concentrations. ACS Omega 2023;8(19):16570–8.
[117] Chen J, Liu T, Chu M, Yu K, Xie X, Lin K, et al. Insight into the interfacial reaction mechanism of FEC and NaF on Na for high performance sodium metal batteries. J Mater Chem A 2024;12(37):25222–32.
[118] Fondard J, Irisarri E, Courrèges C, Palacin MR, Ponrouch A, Dedryvère R. SEI composition on hard carbon in Na-ion batteries after long cycling: influence of salts ($NaPF_6$, NaTFSI) and additives (FEC, DMCF). J Electrochem Soc 2020;167(7):070526.
[119] Wang Z, Hofmann A. NaDFOB and FEC as electrolyte additives enabling improved cyclability of sodium metal batteries and sodium ion batteries. ChemElectroChem 2025;12(5):e202400597.
[120] Liu X, Zhao J, Dong H, Zhang L, Zhang H, Gao Y, et al. Sodium difluoro(oxalato) borate additive-induced robust SEI and CEI layers enable dendrite-free and long-cycling sodium-ion batteries. Adv Funct Mater 2024;34(37):2402310.
[121] Sun Z, Fu W, Liu MZ, Lu P, Zhao E, Magasinski A, et al. A nanoconfined iron(III) fluoride cathode in a NaDFOB electrolyte: towards high-performance sodium-ion batteries. J Mater Chem A 2020;8(7):4091–8.
[122] Wu S, Li Y, Chen L, Zhang Y, Zeng L, Fan H. Hexapod cobalt phosphosulfide nanorods encapsulating into multiple hetero-atom doped carbon frameworks for advanced sodium/potassium ion battery anodes. Chin Chem Lett 2025;36(4):109796.
[123] Lu SJ, Lin JY, Wang CH, Zhang YF, Zhang Y, Fan HS. Heterogeneous engineering of MnSe@NC@ReS_2 core–shell nanowires for advanced sodium-/potassium-ion batteries. Rare Met 2024;43(8):3713–23.
[124] Li H, He Y, Wang Q, Gu S, Wang L, Yu J, et al. $SnSe_2$/$NiSe_2$@N-doped carbon yolk–shell heterostructure construction and selenium vacancies engineering for ultrastable sodium-ion storage. Adv Energy Mater 2023;13(47):2302901.
[125] Xiao Y, Miao Y, Wan S, Sun YK, Chen S. Synergistic engineering of Se vacancies and heterointerfaces in zinc–cobalt selenide anode for highly efficient Na-ion batteries. Small 2022;18(28):2202582.
[126] Zhang Y, Wei S, Zhao Z, Pei X, Zhao W, Wang J, et al. Carbon-encapsulated Ni_3Se_4/$CoSe_2$ heterostructured nanospheres: sodium/potassium-ion storage anode with prominent electrochemical properties. Small 2022;18(14):2107258.
[127] Li Y, Zhang R, Qian J, Gong Y, Li H, Wu C, et al. Construct NiSe/NiO heterostructures on NiSe anode to induce fast kinetics for sodium-ion batteries. Energy Mater Adv 2023;4:0044.
[128] Tang L, Zhang B, Peng T, He Z, Yan C, Mao J, et al. MoS_2/SnS@C hollow hierarchical nanotubes as superior performance anode for sodium-ion batteries. Nano Energy 2021;90(Pt A):106568.
[129] Wang J, Yue X, Cao X, Liu Z, Patil AM, Wang J, et al. Metal organic frameworks derived CoS_2/NiS_2 heterostructure toward high-performance sodium storage anode materials. Chem Eng J 2022;431(Pt 2):134091.
[130] Ma L, Zhou X, Sun J, Zhang P, Hou B, Zhang S, et al. Synergy mechanism of defect engineering in MoS_2/FeS_2/C heterostructure for high-performance sodium-ion battery. J Energy Chem 2023;82:268–76.
[131] Wei S, Li W, Ma Z, Deng X, Li Y, Wang X. Novel bismuth nanoflowers encapsulated in N-doped carbon frameworks as superb composite anodes for high-performance sodium-ion batteries. Small 2023;19(46):2304265.
[132] Ma Y, Lian X, Xu N, Jiang H, Li L, Zhang D, et al. Rational design of few-layer $FePS_3$ nanosheets@N-doped carbon composites as anodes for sodium-ion batteries. Chem Eng J 2022;427:130882.
[133] Li H, Yu G, Luo J, Li G, Wang W, He B, et al. Soft-template-assisted synthesis of petals-like MoS_2 nanosheets covered with N-doped carbon for long cycle-life sodium-ion battery anode. J Electroanal Chem 2022;922:116715.
[134] Yuan X, Chen S, Li J, Xie J, Yan G, Liu B, et al. Understanding the improved performance of sulfur-doped interconnected carbon microspheres for Na-ion storage. Carbon Energy 2021;3(4):615–26.
[135] Xu Y, Zhou M, Wang X, Wang C, Liang L, Grote F, et al. Enhancement of sodium ion battery performance enabled by oxygen vacancies. Angew Chem Int Ed 2015;54(30):8768–71.
[136] Tian Y, Cai Y, Chen Y, Jia M, Hu H, Xie W, et al. Accessing the O vacancy with anionic redox chemistry toward superior electrochemical performance in O3 type Na-ion oxide cathode. Adv Funct Mater 2024;34(32):2316342.
[137] Peng Z, Huang Y, Bannov AG, Li S, Tang L, Tan L, et al. Regulating oxygen vacancies and coordination environment of manganese dioxide for enhanced high-mass-loading energy storage. Energy Environ Sci 2024;17(10):3384–95.
[138] Yang X, Zhang L, Liu G, Pang G, Wang D, Li M, et al. Phase transition modulated by grain size and lattice distortion in layered transition metal oxide for sodium-ion batteries. ACS Appl Mater Interfaces 2024;16(31):40805–13.
[139] Wang Z, Yan X, Wang F, Xiong T, Balogun MS, Zhou H, et al. Reduced graphene oxide thin layer induced lattice distortion in high crystalline MnO_2 nanowires for high-performance sodium- and potassium-ion batteries and capacitors. Carbon 2021;174:556–66.
[140] Li W, Han C, Wang W, Xia Q, Chou S, Gu Q, et al. Stress distortion restraint to boost the sodium ion storage performance of a novel binary hexacyanoferrate. Adv Energy Mater 2020;10(4):1903006.
[141] Zhang T, Ren M, Huang Y, Li F, Hua W, Indris S, et al. Negative lattice expansion in an O3-type transition-metal oxide cathode for highly stable sodium-ion batteries. Angew Chem Int Ed 2024;63(8):e202316949.
[142] Gu ZY, Cao JM, Li K, Guo JZ, Wang XT, Zheng SH, et al. 2D exfoliation chemistry towards covalent pseudo-layered phosphate framework derived by radical/strain-synergistical process. Angew Chem Int Ed 2024;63(30):e202402371.
[143] Zhao XX, Wang XT, Gu ZY, Guo JZ, Cao JM, Liu Y, et al. Unlocking quasi-monophase behavior in NASICON cathode to drive fast-charging toward durable sodium-ion batteries. Adv Funct Mater 2024;34(37):2402447.
[144] Zhao L, Zhang T, Li W, Li T, Zhang L, Zhang X, et al. Engineering of sodium-ion batteries: opportunities and challenges. Engineering 2023;24:172–83.